Summer 7-29-2022

Using Remote and in situ Observations from TORUS to Investigate a Preexisting Airmass Boundary and its Influence on a Tornadic Supercell on 28 May 2019

Kristen Axon
University of Nebraska-Lincoln, kaxon2@huskers.unl.edu

USING REMOTE AND IN SITU OBSERVATIONS FROM TORUS TO INVESTIGATE A PREEXISTING AIRMASS BOUNDARY AND ITS INFLUENCE ON A TORNADIC SUPERCELL ON 28 MAY 2019

by

Kristen Lauren Axon

A THESIS

Presented to the Faculty of

The Graduate College of the University of Nebraska

In Partial Fulfillment of Requirements

For the Degree of Master of Science

Major: Earth and Atmospheric Sciences

Under the Supervision of Professor Adam L. Houston

Lincoln, Nebraska

July 2022

USING REMOTE AND IN SITU OBSERVATIONS FROM TORUS TO INVESTIGATE A PREEXISTING AIRMASS BOUNDARY AND ITS INFLUENCE ON A TORNADIC SUPERCELL ON 28 MAY 2019

Kristen Lauren Axon, M.S.

University of Nebraska, 2022

Advisor: Adam L. Houston

During the 2019 field phase of Targeted Observation by Radars and UAS of Supercells (TORUS), a preexisting airmass boundary was sampled on 28 May 2019 in north-central Kansas in close proximity to a tornadic supercell. This work hypothesized that the preexisting airmass boundary was associated with a mesoscale air mass with high theta-E (MAHTE) that favorably interacted with the tornadic supercell to increase the likelihood of tornadogenesis. Observations from TORUS including mobile mesonets, unoccupied aerial vehicles, soundings, and ground-based mobile radar were used along with GOES-16 visible satellite imagery, Kansas mesonet surface stations, and KUEX WSR-88D data to investigate this hypothesis.

Analysis revealed that the preexisting airmass boundary was associated with a synoptic-scale warm front and the cool air mass associated with this boundary had higher moisture compared to the warm side environment resulting in a higher equivalent potential temperature within the cooler air mass. This MAHTE had a boundary-normal width of around 13 km and a vertical depth around 400 m meaning it was truly mesoscale in size. The environment within the MAHTE had similar MLCAPE, greater vertical wind shear, and a lower lifting condensation level than the warm side environment rendering it more favorable for tornadic supercells.

A storm-scale analysis of the evolution of the tornadic supercell, a nontornadic supercell that developed within the MAHTE to the northeast of the tornadic storm, and the preexisting airmass boundary indicated that the preexisting airmass boundary likely interacted with the tornadic supercell in a way that promoted tornadogenesis. The nontornadic supercell also produced at least two outflow boundaries that interacted with the tornadic storm, one of which had a very stable air mass behind it and is hypothesized to have weakened the tornadic supercell.

Acknowledgements

Acknowledgements are owed to my advisor Dr. Adam Houston, and my committee members Dr. Matthew Van Den Broeke and Dr. Clint Rowe for guiding me through my Masters research and providing support throughout the duration of this project. I would also like to thank Matthew Wilson for helping me get started with coding analysis and being available to discuss ideas and troubleshoot Python errors. I give my thanks to members of the Severe Storms Research Group for providing feedback on my work and many insightful discussions. I also want to acknowledge everyone who participated on TORUS 2019 and collected the many datasets I have used in this work. Other thanks are given to Bobby Jackson, Matt Wilson, Alex Scheuth, Elizabeth Venticher, and Tony Reinhart, for helping with different aspects of my analysis. Finally, I would like to thank my family and friends for their incredible support throughout this project.

This work was made possible through the National Science Foundation award #1824649 and the Earth and Atmospheric Sciences Department at the University of Nebraska-Lincoln.

Table of Contents

List of Figures

List of Tables

Chapter 1: Introduction

The interaction between preexisting airmass boundaries and supercells is known to support storm intensification, storm longevity, and tornadogenesis (Maddox et al. 1980; Markowski et al. 1998; Atkins et al. 1999; Johns et al. 2000; Rasmussen et al. 2000; Groenemeijer et al. 2011; Laflin and Houston 2012; Honda and Kawano 2016). Synoptic fronts and remnant thunderstorm gust fronts can be associated with localized environments favorable for tornadic supercells with conditions such as high boundary layer relative humidity and both vertical and horizontal vorticity located within a narrow region along a boundary (Maddox et al. 1980). Previous research has highlighted a meaningful relationship between preexisting boundaries and tornadic supercells (Markowski et al. 1998; Rasmussen et al. 2000; Honda and Kawano 2016) with nearly 70% of significant tornadoes intercepted during the Verifications of the Origins of Rotation in Tornadoes Experiment (VORTEX) occurring near boundaries (Markowski et al. 1998). Boundaries are often recognized as regions of interest by forecasters as they can also contribute to the development of mesovortices in quasi-linear convective systems (Wheatley and Trapp 2008). In general, though, the subject of supercells associated with environmental heterogeneities (e.g., supercells interacting with boundaries, supercells modifying their environment) is an area of research that remains relatively incomplete (Markowski and Richardson 2009).

Recent studies have also focused on a specific type of air mass associated with some boundaries known as a mesoscale air mass with high theta-E (MAHTE; Hanft and Houston 2018). A MAHTE forms on the immediate cool side of boundaries and is characterized by having higher equivalent potential temperature (θ_e) relative to the warm

side environment. It is considered meso-γ scale (Rasmussen et al. 2000; Groenemeijer et al. 2011) so current observation networks and numerical models usually lack sufficient spatial resolution to appropriately discern MAHTEs. A primary example of this possibly occurred on 28 May 2019.

During the 2019 field phase of Targeted Observation by Radars and UAS of Supercells (TORUS; Houston et al. 2020), a tornadic supercell was sampled by a multitude of instrumented platforms on 28 May 2019 near Tipton, KS. Also sampled was a preexisting airmass boundary hypothesized to be a warm front that extended across northeast Kansas and transitioned to a quasi-stationary front into northern Missouri from a low-pressure system over west-central Kansas. Mobile mesonets measured a modest increase (2-3 K) in dewpoint on the immediate cool side when crossing this boundary. Another storm also occurred in close proximity to this boundary which formed rapidly and became supercellular but not tornadic. It is hypothesized that the preexisting airmass boundary and accompanying cool air mass provided an optimal, but spatially limited, environment for the tornadic supercell due to favorable thermodynamics and kinematics. This research also hypothesizes that the air mass behind the boundary represented a MAHTE given the higher moisture present on the cool side.

In order to gain a more detailed perspective into the air masses ahead of and behind the boundary in this work, observations collected by unoccupied aerial vehicles (UAVs) operating alongside more standard instrumentation used in field campaigns that target supercells and tornadoes (i.e. mobile mesonets, mobile ground based radar, and mobile sounding launch sites) are examined. Previous observational studies of tornadic supercells in proximity to boundaries primarily relied on in situ observations near the

surface (e.g., Markowski et al. 1998; Rasmussen et al. 2000; Groenemeijer et al. 2011) except for vertical profiles taken by radiosondes which have a limited ability to make targeted measurements. Since UAVs are piloted remotely, specific regions of a supercell can be targeted where observations are relatively uncommon providing a new interpretation on the near-storm and in-storm environment of supercells (Elston et al. 2011). Finally, the characteristics of the warm air mass, cool air mass, and environment immediately above the boundary can begin to be differentiated in greater detail.

This research investigates a preexisting airmass boundary using both in situ and remote observations collected during TORUS on 28 May 2019 to examine its characteristics and determine its potential influence on a tornadic supercell. Anticipating how a storm may evolve when interacting with environmental heterogeneities is crucial to improving warning lead times for severe hazards and reducing false alarm rates (NWS 2021a). This work provides insights into the influence environmental heterogeneities can have on the evolution of a supercell including both constructive and deconstructive interactions.

Chapter 2: Background

2.1 Relevant Literature

a. Preexisting Airmass Boundaries Interacting with Supercells

Previous works have noted that as supercells approach preexisting airmass boundaries, there is an increase in tornado occurrence (Maddox et al. 1980; Atkins et al. 1999; Rasmussen et al. 2000; Magee and Davenport 2020). Maddox et al. (1980) developed a theoretical model of boundary layer vertical wind profiles across typical synoptic-scale airmass boundaries associated with severe weather. A favorable zone between a warm moist air mass and cooler moist air mass is characterized by a region of cyclonic vorticity, convergence, and a narrow mixing zone which promotes an environment favorable for tornadic supercells (Fig. 2.1; Maddox et al. 1980). At a much smaller scale, as storms interact with airmass boundaries they encounter additional baroclinic horizontal vorticity generated from buoyancy gradients on the immediate cool side of the boundary (Markowski et al. 1998; Atkins et al. 1999; Rasmussen et al. 2000; Laflin and Houston 2012). This horizontal vorticity is considered the predominant means by which storms interacting with boundaries obtain or strengthen low-level rotation and increase the likelihood for tornadogenesis (Markowski et al. 1998; Atkins et al. 1999; Rasmussen et al. 2000). A conceptual model presented in Markowski et al. (1998) exhibits this process which promotes low-level mesocyclogenesis and amplifies stretching near the surface (Fig. 2.2; Markowski et al. 1998).

To better understand the relationship between airmass boundaries and low-level rotation, two numerical studies performed backward trajectories on supercells interacting

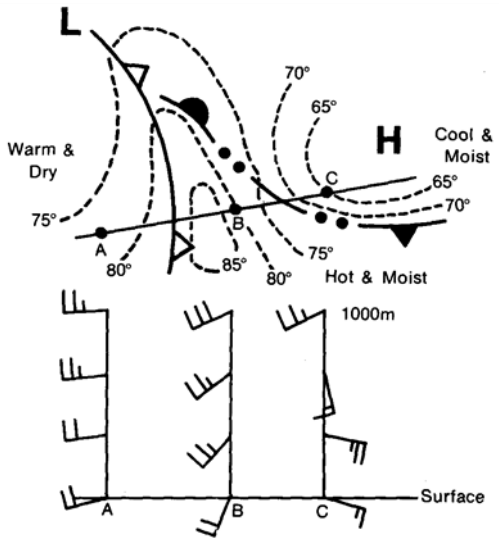

Figure 2.1: Schematic of the boundary layer wind profiles across boundaries typical for severe weather setups taken from Maddox et al. (1980). The region across points B (characterized as a hot and conditionally unstable air mass) and C (characterized as cool and stable thunderstorm outflow) represent a region with cyclonic vorticity, convergence, and a mixing zone which generally support rotating thunderstorms.

with boundaries to determine where parcels entering the low-level mesocyclone originated (Atkins et al. 1999; Laflin and Houston 2012). Both studies found that the majority of these parcels originate from the cool air mass behind the boundary and experience horizontal vorticity enhancement as they travel through the cool air before being tilted by the storm's updraft. Once in the updraft, these parcels are then stretched, increasing positive vertical vorticity within the updraft and near the surface. However, the likelihood of tornadogenesis and the track length of tornadoes generally depend on the orientation of the boundary relative to the storm's motion (Atkins et al. 1999; Magee and Davenport 2020).

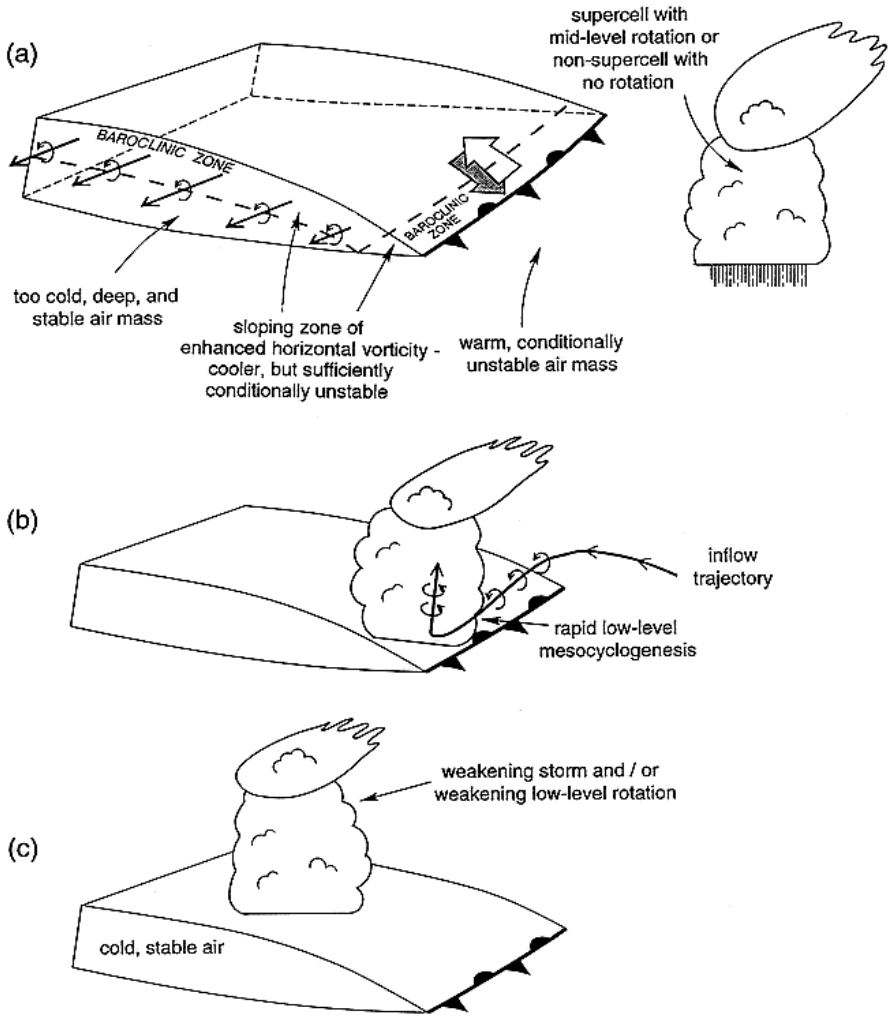

Figure 2.2: A conceptual model from Markowski et al. (1998) illustrating the development of a low-level mesocyclone from baroclinic horizontal vorticity generated behind a boundary. This vorticity becomes ingested into a storm's updraft resulting in low-level rotation.

Both Atkins et al. (1999) and Magee and Davenport (2020) determined that when a storm moves parallel to a boundary, tornadogenesis is more likely and longer-lived tornadoes tend to occur. Atkins et al. (1999) conducted numerical boundary orientation experiments based on a tornadic supercell from 16 May 1995 near Garden City, KS, to determine the sensitivity of the evolution of the simulated supercell. Experiments with an orientation angle greater (less) than 62° resulted in the supercell crossing the boundary into the cool (warm) side while at or near 62°, the storm propagated along the boundary.

Figure 2.3 (Atkins et al. 1999) compares the maximum vertical vorticity (ζ_{max}) and maximum vertical motion (W_{max}) from each experiment; both values are maximized when the supercell motion is nearly parallel to the boundary. In Magee and Davenport (2020), they examined 90 supercells and associated severe weather reports in various proximities to different boundary types (stationary fronts, warm fronts, and outflow boundaries), where tornadoes were found to occur close to boundaries ($\leq$ 40 km) and when the parent storm moved nearly parallel to the boundary and/or towards the cool side. Storms propagating along boundaries have sustained access to the additional baroclinic horizontal vorticity associated with the boundary allowing for more persistent rotation to be maintained (Markowski et al. 1998).

It is hypothesized that storms that continue farther into the cool air mass and interact with increasingly stable air weaken as parcels become less buoyant suppressing vertical motion over time (Fig. 2.2; Markowski et al. 1998). This would explain why tornadoes are often shorter lived when the parent storm crosses the boundary instead of moving along it. In some cases, though, the cool air mass is less detrimental, such as on 2 June 1995 (Rasmussen et al. 2000; Gilmore and Wicker 2002). During this event, storms that either crossed or initiated and remained on the cool side of a preexisting outflow boundary developed the strongest low-level rotation, even 50 km into the cool air, compared to storms on the warmer side (Fig. 2.4; Rasmussen et al. 2000).

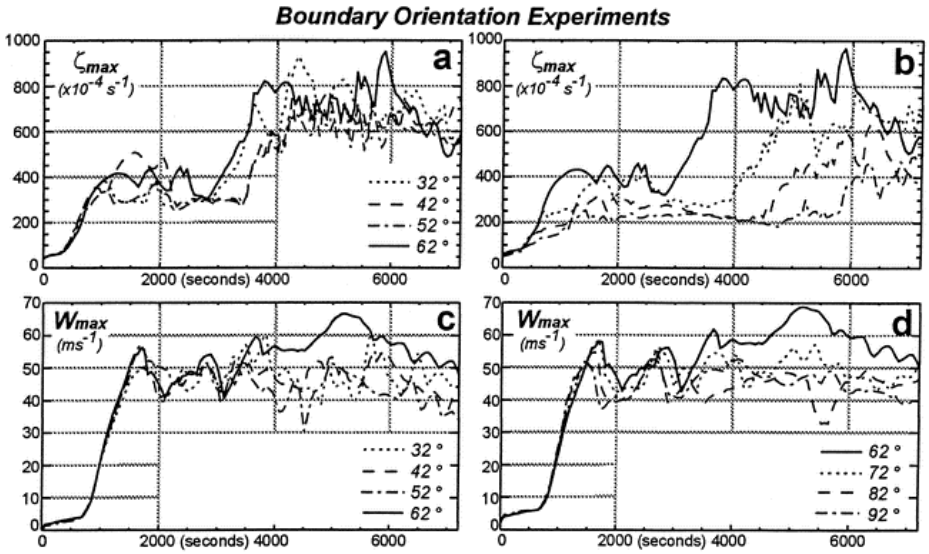

Figure 2.3: From Figure 5 in Atkins et al. (1999), these plots are time series of maximum low-level vertical vorticity (ζ_{max}; $\zeta \times 10^{-4}$ s^{-1}) and maximum vertical velocity (W_{max}; m s^{-1}) anywhere in the model domain for all boundary runs. The orientation of the storm interaction with the boundary is represented by varying angles. For angles greater (less) than 62° in panels a and c (b and d), the supercell crossed the boundary into the cool (warm) side. For an angle of 62°, the supercell propagated along the boundary. In a-d, the parallel movement (solid curve) resulted in generally the highest ζ_{max} and W_{max} in the model domain from 0 to 7000 seconds.

Baroclinic horizontal vorticity produced by the boundary along with modestly enhanced vertical vorticity and enhanced convective available potential energy (CAPE) on the immediate cool side were considered the primary factors resulting in significant tornadoes (F2+) (Rasmussen et al. 2000). Mobile mesonet data and proximity soundings revealed higher low-level moisture and low-level vertical wind shear in a 40 km wide band on the cool side of the boundary supporting substantial instability and low-level storm-relative helicity (SRH) within this region (Gilmore and Wicker 2002).

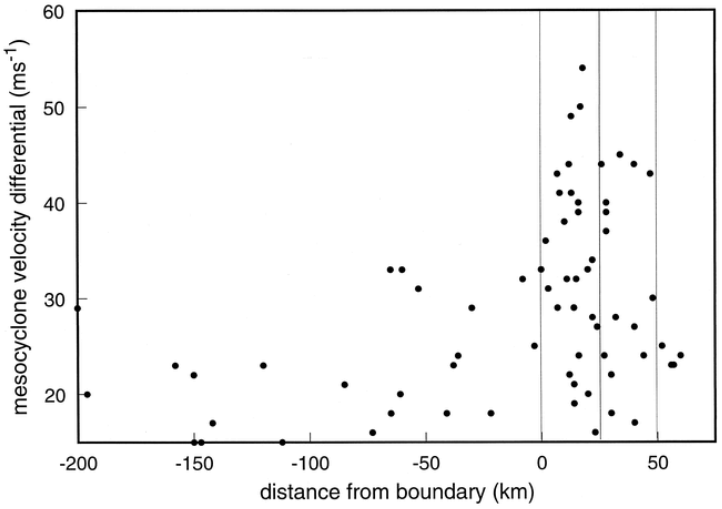

Figure 2.4: Figure 10 from Rasmussen et al. (2000) showing low-level mesocyclone strengths (differential velocity – difference between inbound and outbound Doppler radial velocity peaks on base scan) vs distance from a prominent boundary (positive towards cooler air). Each dot represents one detection; all data at 10-min intervals are included.

Similarly, Guyer and Ewald (2004) documented the rapid intensification of storms on 22 June 2003 as they initiated on the cool side of an outflow boundary that developed from earlier convection in central Nebraska. Surface observations indicated moisture was higher in the cooler air mass and three F0 tornadoes and large hail up to 7 inches occurred with these storms. On 28 July 2005, these same conditions transpired within the cool side of a warm front in Birmingham, United Kingdom where three tornadoes occurred (Groenemeijer et al. 2011). The narrow zone on the immediate cool side was investigated to understand why it was a favorable region for tornadoes despite cooler temperatures. Ultimately, the environment on the immediate cool side of the warm front had higher dewpoint temperatures relative to the warm side resulting in greater $\boldsymbol{\theta}_e$, higher surfaced-based CAPE (SBCAPE), and greater 0-1 km bulk shear (Fig. 2.5; Groenemeijer et al. 2011).

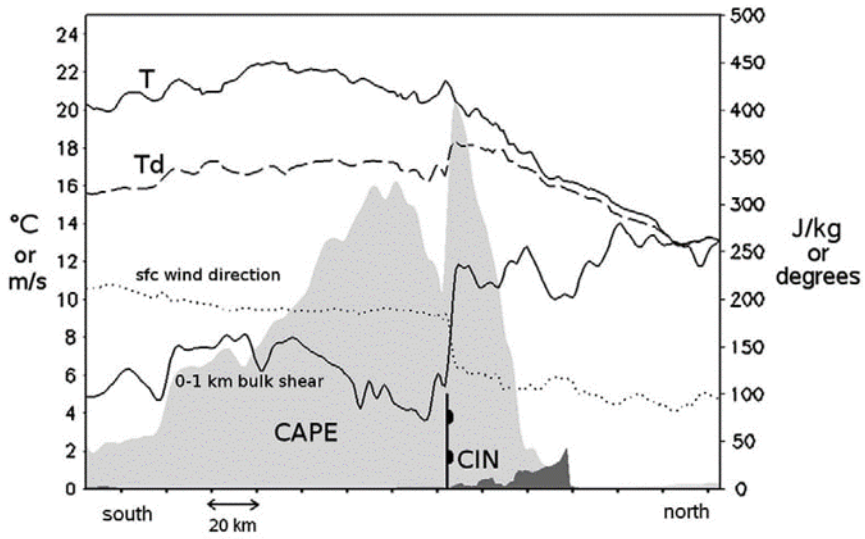

Figure 2.5: Taken from Figure 15 in Groenemeijer et al. (2011) is a north–south cross-section of several parameters at 1300 UTC across the warm front: temperature at 1000 hPa (continuous line, top; °C), dew point temperature (dashed line; °C), wind direction at 10 m AGL (dotted, degrees), 0–1 km bulk shear (continuous line, m s^{-1}), SBCAPE (light shading) and CIN (dark shading) for a parcel lifted from 1000 hPa.

These cases represent examples of supercells interacting favorably with a boundary and an associated cool air mass representative of a MAHTE suggesting a constructive relationship and supporting the notion that conditions present in a MAHTE (i.e. higher moisture, instability, and low-level SRH) are particularly favorable for storms initiating or entering that air mass. Had these air masses not had characteristics of a MAHTE, would the same events have unfolded? While this question is unanswerable, it deserves further investigation as more examples of MAHTEs interacting with supercells are examined to further understand their effect and improve the ability to predict how a storm may evolve when interacting with this type of air mass.

b. MAHTEs

Boundaries with associated air masses exhibiting characteristics of a MAHTE have been documented in several observational works investigating the role of boundary interactions with tornadic supercells (Rasmussen et al. 2000; Gilmore and Wicker 2002; Guyer and Ewald (2004); Groenemeijer et al. 2011). While the characteristics of MAHTEs are evidently important for supercell development and tornadogenesis, a study by Hanft and Houston (2018) also explored what processes lead to their initial formation by using a numerical simulation to model the development and evolution of a MAHTE that occurred on 20 June 2016 along a cold front in northwest Kansas. Observations from a mobile mesonet showed that higher values of θ_e extended 40-50 km into the cool side with a maximum θ_e perturbation, relative to the warm sector, of 15-20 K immediately behind the boundary. These conditions resulted in the cool air mass having greater SBCAPE and lower LCLs than the warm air mass.

Using the Advanced Research Weather Research and Forecasting (WRF-ARW) model to simulate this environment, Hanft and Houston (2018) determined that a MAHTE can form due to differences in the stability of air masses across a boundary which result in the differential vertical advection of moisture. The cooler side, which is initially more stable earlier in the day, becomes more resistant to mixing from daytime heating. On the warm side, drier air aloft advects down into the planetary boundary layer reducing the overall moisture content in this air mass. This additional moisture on the cool side offsets the negative impact of cooler temperatures rendering it more unstable relative to the warm air mass.

To date, MAHTEs documented in the literature share common characteristics relative to warm sector environmental conditions including cooler temperatures, higher moisture, higher instability, and greater vertical wind shear more supportive for supercells. However, broadly accepted criteria for MAHTE identification have not been established. For this study, we will assume that an air mass that is cooler and has a higher θ_e than the warm side environment of a boundary, and maintains these conditions in a boundary-normal direction at the mesoscale *O*(2-200 km) represents a MAHTE.

c. UAV Observations in Supercell Studies

The use of UAVs in atmospheric observation is a relatively new area of research, especially in regards to supercells interacting with environmental heterogeneities like airmass boundaries. On 30 September 2009, Houston et al. (2012) sampled two airmass boundaries, a cold front and thunderstorm generated gust front, but predominantly focused on addressing the practicality of utilizing small unoccupied aircraft operating semi-autonomously. During the Verification of the Origins of Rotation in Tornadoes Experiment (VORTEX2; Wurman et al. 2012), the first UAV measurements within the rear-flank downdraft (RFD) of a tornadic supercell were obtained but concentrated on internal structures hypothesized to occur within rear-flank outflow (Elston et al. 2011; Riganti and Houston 2017). No prior study has specifically examined the interaction between an airmass boundary and supercell using UAV observations. Major benefits to using UAVs involve their ability to target specific regions of interest, flexibility in sampling strategy, and obtaining observations in areas dangerous for people.

Since supercell evolution is a function of the storm's local environment, projects such as TORUS that sample these environments with a dense network of observations resolve local conditions fairly well, especially with the addition of UAVs. The meteorological surveillance network is generally too sparse to resolve this local environment, particularly in the presence of small-scale environmental heterogeneities like those associated with airmass boundaries. In general, the parameters deemed to best differentiate tornadic from nontornadic environments relate to boundary layer moisture and low-level winds, e.g., LCL, CAPE, and low-level SRH (Thompson et al. 2003). Heterogeneities in these parameters are typical of airmass boundaries.

Distinguishing between tornadic and nontornadic supercells has been a long-established challenge for forecasters and is further complicated by changes to local environments in association with heterogeneities like those corresponding with boundaries. It is also likely that we have an incomplete understanding of the sensitivity of supercells and tornadoes to the ambient environment. The purpose of this work is to characterize the environmental heterogeneity associated with an observed boundary near (in both space and time) its interaction with a supercell. The 28 May 2019 tornadic supercell had a relatively dense network of observations from TORUS with the unique addition of UAVs providing information farther aloft on the thermodynamics and kinematics of the air masses influencing this storm. The principal objectives in this study are:

1. Characterize the thermodynamic and kinematic properties of the warm and cool air masses associated with the preexisting airmass boundary.

2. Use storm-scale analysis to infer the possible role of the preexisting airmass boundary on the tornadic supercell.

2.2 Case Overview

The synoptic environment on 28 May 2019 supported the potential for severe storms including the possibility of tornadoes with an upper-level trough over the western United States and a warm front across northeast Kansas becoming a quasi-stationary front into northern Missouri. The front became the focus for storm initiation, with the most prominent severe weather threat anticipated in northern Missouri. Throughout the day, cloud cover remained north of the warm front while the warm sector became mostly clear by 1900Z after early morning convection moved out of the area over central to northeastern Kansas.

On visible satellite imagery, a line of cumulus clouds developed along the front around 1820Z defining its location across Kansas (Fig. 2.6a). Observations on both sides of this cumulus line indicated the different conditions across the front. For example, a surface observation just south of the cumulus line within the warm sector measured a 79°F (26°C) temperature and 68°F (20°C) dewpoint with southerly winds around 10 knots while another observation farther west and at the line of cumulus observed a 75°F (24°C) temperature and 70°F (21°C) dewpoint with northeasterly winds around 10 knots (Fig. 2.6a).

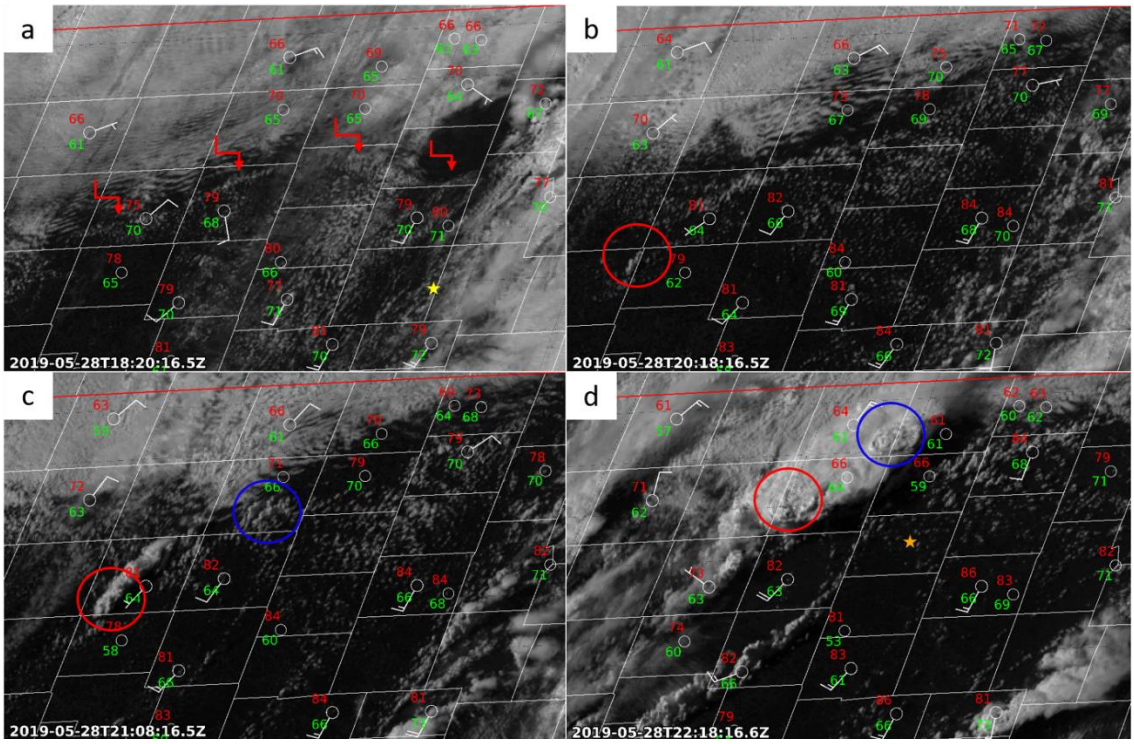

Figure 2.6: GOES-16 visible satellite imagery over north-central Kansas overlaid with Kansas mesonet surface station plots with temperature in Fahrenheit (dewpoint in Fahrenheit) in the top (bottom) left corner in red (green) at a) 1820Z, b) 2018Z, c) 2108Z, and d) 2218Z. Wind barbs are in knots. In (a), the red arrows highlight the line of cumulus clouds developing along a warm front. In (b-d), the red circle highlights towering cumulus associated with the Tipton supercell and the blue circle highlights towering cumulus associated with the nontornadic supercell. The yellow (orange) star demarcates the location of a TORUS sounding at 1931Z (2219Z).

At 1931Z (see yellow star in Fig. 2.6a for location), a TORUS sounding showed MLCAPE of 3746 J kg^{-1} and near-zero mixed-layer convective inhibition (MLCIN) of -0.87 J kg^{-1} within the warm sector (Fig. 2.7). However, the vertical wind profile lacked directional shear resulting in low-level SRH unfavorable for tornadic supercells. 0-1 km SRH was 79 $m^2 s^{-2}$ while 0-1 km SRH > 100 $m^2 s^{-2}$ is considered favorable for tornadic supercells (Thompson et al. 2003).

Around 2018Z, towering cumulus began developing that would evolve into the supercell that later produced an EF2 tornado near Tipton, KS (referred to as the Tipton

supercell from this point on; Fig. 2.6b). By 2108Z, KUEX, the Weather Surveillance Radar-1988 Doppler (WSR-88D) in Blue Hills, NE, observed reflectivity values associated with the Tipton storm increasing to 52 dBZ. At this time, it remained nonsupercellular, and a second storm initiated to the northeast (Fig. 2.6c), later becoming a nontornadic supercell. Local storm reports viewed through the Gibson Ridge GR2Analyst Version 2 analysis application indicate a landspout on the Tipton supercell at 2114Z leading to the first tornado warning for this storm. Both storms displayed overshooting tops around 2218Z (Fig. 2.6d) and exhibited rotation with reflectivity hook echoes. Around 2220Z, a tornado was reported on the Tipton supercell along with damage. At this same time, a second TORUS sounding was released east of the Tipton storm in the far field environment though a full profile was not obtained (Fig. 2.8; see orange star in Fig. 2.6d for location). The MLCAPE up to last observation indicates instability remained sufficient, but more importantly the 0-1 km SRH remained the same as earlier and was still below the threshold considered supportive for tornadic supercells even though a tornadic supercell was occurring in this environment.

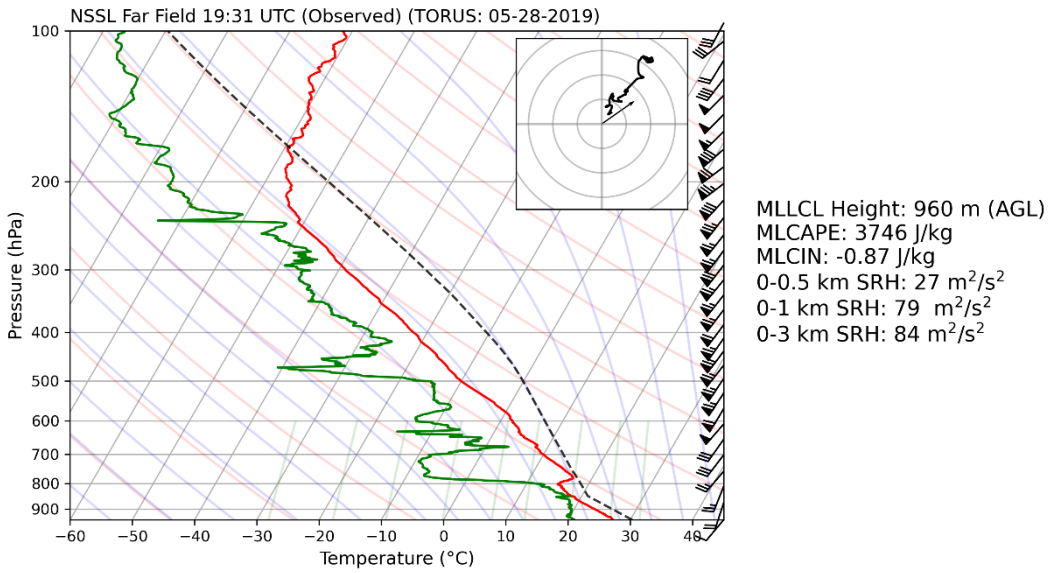

Figure 2.7: 1931 UTC NSSL sounding on 28 May 2019. Hodograph rings are at 10 m s^{-1} intervals. Storm motion vector is based on the Tipton supercell's observed storm motion of 16.5 m s^{-1} from 235°.

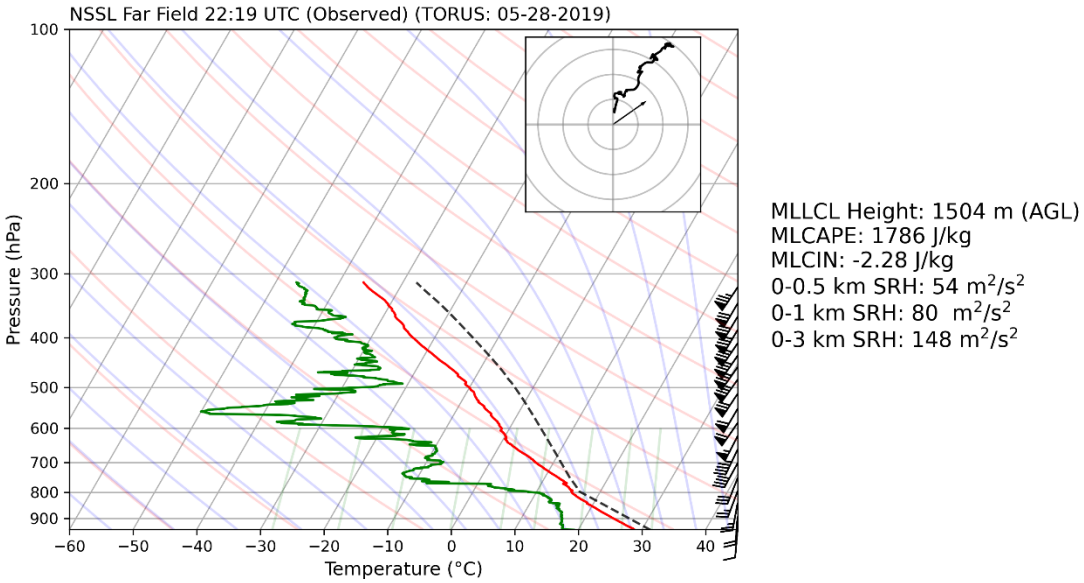

Figure 2.8: Same as Fig. 2.7 except at 2219 UTC.

While conventional methods for monitoring this convection were mostly effective, not all atmospheric conditions that may have contributed to the evolution of these storms were evident. Even the additional TORUS soundings obtained in the near-storm environment did not fully capture the low-level environment that may have influenced the Tipton supercell. Through additional platforms utilized during TORUS, a more in-depth investigation of the low-level thermodynamic and kinematic characteristics is revealed along with a more thorough examination of the storm's evolution.

Chapter 3: Methodology

3.1 In Situ Observations

On 28 May 2019, almost every in situ platform involved with TORUS (Houston et al. 2020) actively collected coordinated observations allowing for extensive coverage of the far-field and near-storm environments of the Tipton and nontornadic supercells. A timeline showing the operation period of each instrument used in this analysis is presented in Figure 3.1. The University of Nebraska-Lincoln (UNL) operated three Combined Mesonet and Tracker (CoMeT) vehicles (denoted CoMeT-1, CoMeT-2, and CoMeT-3) with instrument sensor details provided in Table 3.1 (Houston et al. 2021a,b,c). Similarly, the NSSL operated two dedicated mobile mesonets (Probe-1, Probe-2; Waugh 2020a) and two mobile mesonets equipped to launch soundings (Far-Field - FFld; Waugh 2020a,b and LIDAR; Smith and Coniglio 2019). All surface observation instrument sensor details are provided in Table 3.2.

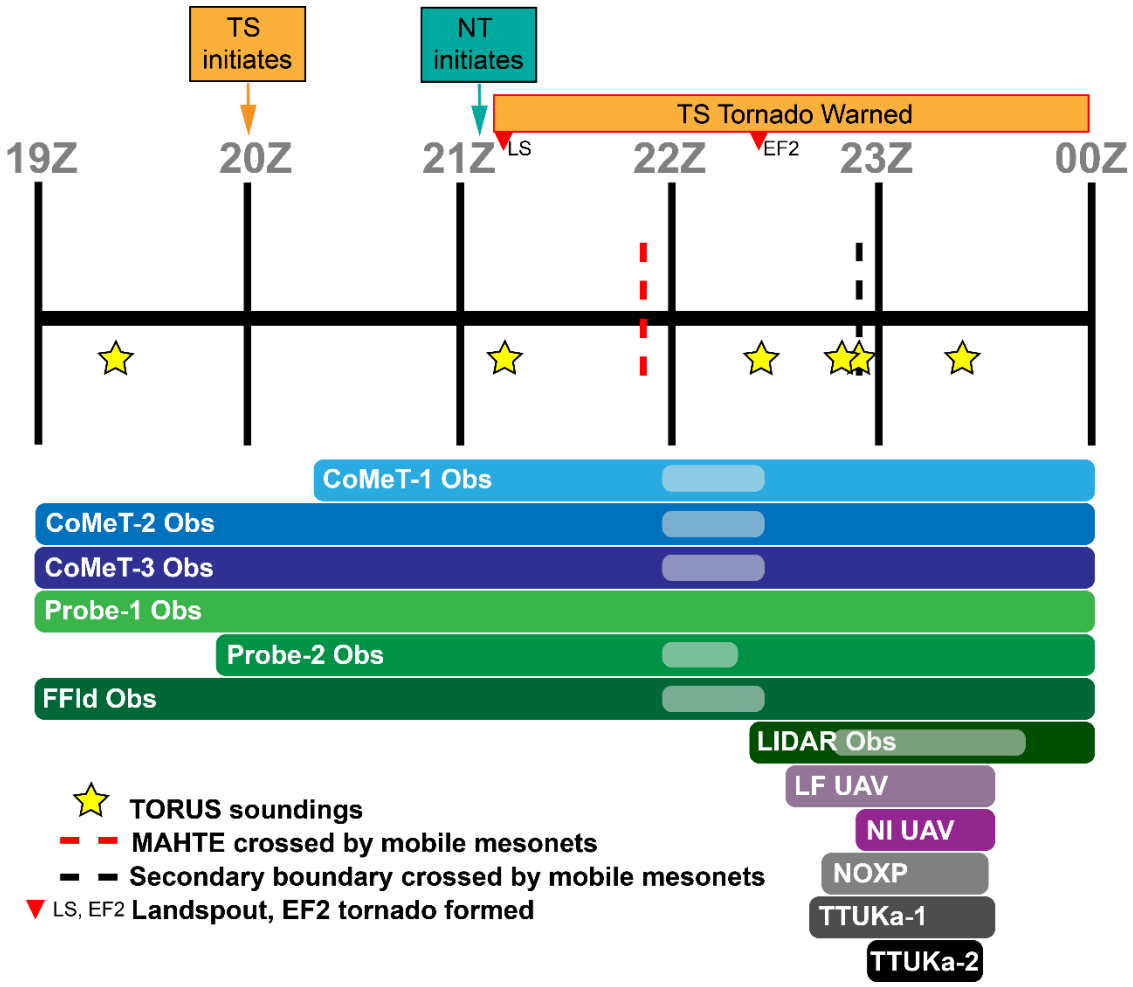

Figure 3.1: Timeline of TORUS instrument operations on 28 May 2019. TS represents the Tipton (tornadic) supercell and NT represents the nontornadic supercell. The gray rounded rectangles demarcate when mobile mesonet vehicles were stationary. TORUS soundings (stars), the time when the MAHTE was crossed by mobile mesonets (red dashed line), the time when the secondary boundary was crossed by mobile mesonets (black dashed line), the times when the tornadic (orange box) and nontornadic (teal box) storms initiated, the time when the landspout and the EF2 tornadoes formed (red triangles labeled LS and EF2 respectively), and the duration of the Tipton storm being tornado warned (orange box with red outline) are shown. Note that some platforms operated outside of the time period shown.

Table 3.1: Information on sensors used on the CoMeT vehicles. CoMeT-2 and CoMeT-3 have different sensor models for RH and slow temperature from CoMeT-1 while all other sensor models are the same for all three vehicles.

Component	Model	Output	Accuracy
RH and slow-temperature (CoMeT -1)	Vaisala HMP155A-L20-PT	Temp: -80 to +60 °C RH: 0 to 100%	Temp: ±(0.226 - 0.0028 × temperature)°C RH: ±(1.0 + 0.008 × reading) % RH Response time: 20 s
RH and slow-temperature (CoMeT -2 & CoMeT-3)	Vaisala HMP155E		
Fast temperature	Campbell Scientific 109SS-L Thermistor	-40 to +70 °C	± 0.1 °C Response time: 7.5 s (3 m s^{-1})
Pressure	Vaisala PTB210	500-1100 hPa	± 0.25 hPa
Wind	RM Young 01053-L20-PW Propeller-vane Anemometer	WS: 0 to 100 m s^{-1} WD: 0 to 360 °	WS: ± 1% WD: ± 3°

Table 3.2: Information on surface observation sensors used on the NSSL vehicles.

Component	Model	Output	Accuracy
RH and slow-temperature	HMP155	Temp: -80 to +60 °C RH: 0.8 to 100%	Temp: ±(0.226 + 0.0028 * temperature) °C (-80°C to +20°C) ±(0.055 + 0.0057 * temperature) °C (+20°C to +60°C) RH: ±0.6% (0% to 40% RH); ±1% (40% to 97% RH) Response time: 20 s
Fast temperature	109SS	-40 to +70 °C	± 0.02 °C
Pressure	PTB210	500-1100 hPa	Linearity: ±0.1 hPa Hysteresis: ±0.05 hPa Repeatability: ±0.05 hPa
Wind	RM Young 05103 Wind Monitor	WS: 0 to 100 m s^{-1} WD: 0 to 360 °	WS: ± 1% WD: ± 3°

Two Robust Autonomous Aerial Vehicle-Endurant Nimble (RAAVEN) UAVs were operated by the University of Colorado, Boulder (Frew et al. 2020) for this case (Fig 3.2). The fixed-wing aircraft housed a multi-hole probe (MHP) sensor to measure pressure, temperature, and relative humidity. Assuming a first-order sensor, similar to the approach of Miloshevich et al. (2004), a time response correction of 11 seconds has been

applied to the temperature and humidity data due to a slower sensor response time. MHP temperature and humidity measurements can also be impacted by heating from full sun and evaporative cooling in rain. However, visible satellite imagery reveals considerable anvil shadowing during data collection where TORUS was operating, and radar reflectivity overlaid with the UAV locations indicates neither aircraft flew within precipitation. The UAV observations used in vertical profiles were sorted by height subsampled every 6.75 meters.

The MHP sensor also observed the three-dimensional winds which were calibrated during post-processing, however this lead to erroneous winds particularly for the NI UAV observations. Figure 3.3 compares the calibrated horizontal UAV winds to the winds observed by the autopilot sensor (PixHawk Cube) along with the low-level winds from a sounding launched by the LIDAR vehicle that was released around the same time and location as the NI UAV. While the LF UAV calibrated and autopilot winds have a similar magnitude and curvature in the hodograph, the NI UAV calibrated winds have a higher magnitude and more variable direction that appears unrealistic compared to the NI UAV autopilot winds. Moreover, the NI UAV autopilot winds have a very similar magnitude and curvature to the LIDAR winds. Because the NI UAV autopilot winds are more reasonable, the vertical profiles from both UAVs use the autopilot observed winds.

RAAVEN-3 (referred to as the LF UAV) primarily executed horizontal transects while following the positions of CoMeT-1 and CoMeT-3 north/northeast of the Tipton supercell’s mesocyclone while RAAVEN-4 (referred to as the NI UAV) performed

vertical profiles in the near-inflow environment generally 13-30 km east of the mesocyclone.

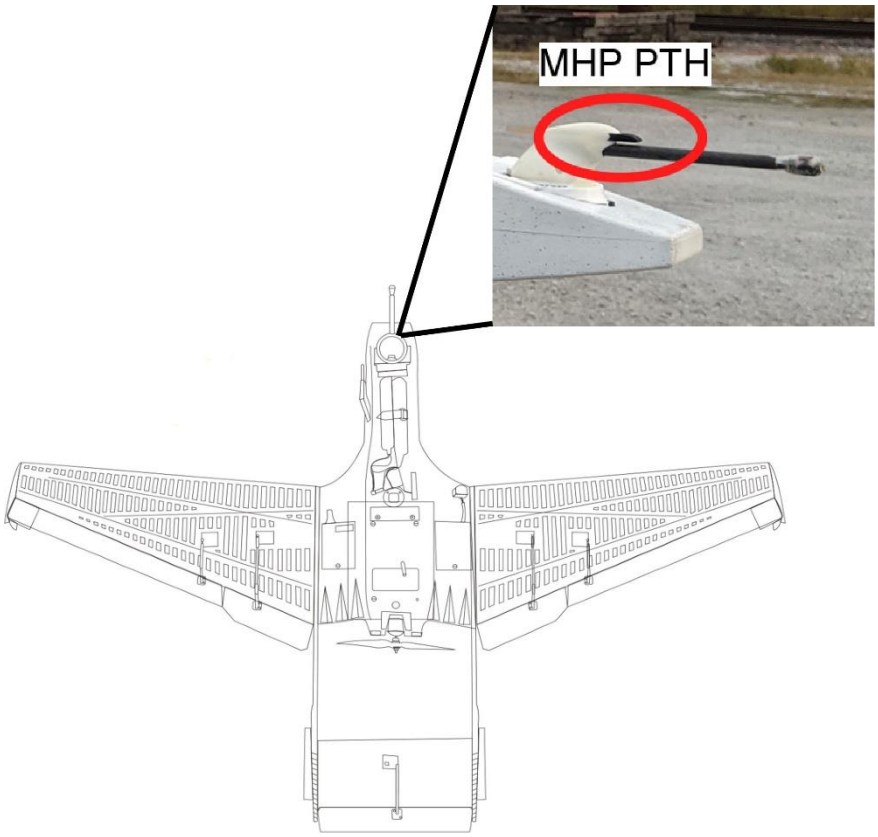

Figure 3.2: RAAVEN schematic with a photo of the multi-hole probe sensor (labeled as MHP PTH in a red oval). The MHP sensor measures pressure, temperature, relative humidity, and the 3-dimensional winds.

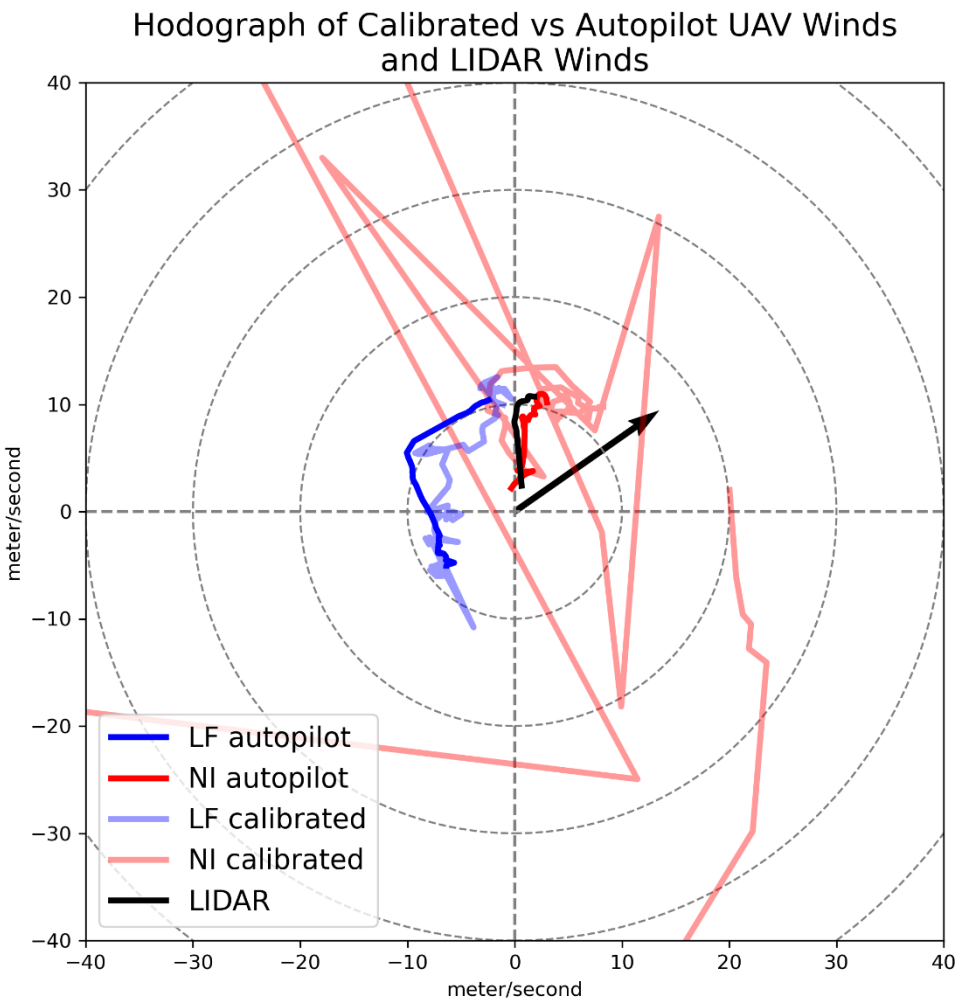

Figure 3.3: Hodograph of the LF UAV autopilot winds (solid blue curve), NI UAV autopilots winds (solid red curve), LF UAV calibrated winds (faded solid blue curve), NI UAV calibrated winds (faded solid red curve), and LIDAR sounding winds (solid black curve). Hodograph rings are at 10 m s^{-1} intervals. Storm motion vector (black arrow) is based on the Tipton supercell's observed storm motion of 16.5 m s^{-1} from 235°.

3.2 Mobile Radars

Three mobile research radars operated during this case: the NOAA X-band dual-polarimetric Doppler radar (NOXP; Burgess et al. 2020) and two Ka-band radars from Texas Tech University (denoted as TTUKa-1 and TTUKa-2; Weiss and Schueth 2019) (Table 3.3). NOXP performed deep planned-positioned-indicator (PPI) scans while the

TTUKa radars implemented shallow PPI scans with a range height indicator taken between each PPI scan. During this case, the 0-1° elevation tilts captured the preexisting airmass boundary making these levels the focus for analysis. Radial velocities for all radars were dealiased using the Python Atmospheric Radiation Measurement Radar Toolkit (Py-ART; Helmus and Collis 2016), and NOXP had some noise removed for gates with a normalized coherent power value below 0.3 (A. Reinhart 2022, personal communication).

Table 3.3: NOXP and TTUKa radar specifications on 28 May 2019 and nominal operational characteristics during the 2019 field phase of TORUS.

Specification	**NOXP**	**TTUKa**
Latitude	39.3499°N	39.4957°N
Longitude	-98.1163°W	-98.1166°W
Altitude	458 m (MSL)	448 m (MSL)
Band	X	Ka
Half-power beamwidth	0.88°	0.33°
# sweeps per volume	18(0.5-20°)	2(0.0-0.5° or 0.5-1°)
Nyquist velocity	19.14 m s^{-1}	15.05 m s^{-1}
Maximum unambiguous range	62.46 km	21.41 km

Both radars were gridded to the same Cartesian coordinate system in Py-ART using a single-pass Barnes objective analysis weighting scheme (Barnes 1964) following the recommendation of Pauley and Wu (1990) where $\boldsymbol{\kappa} = (1.33d)^2$ and d is the coarsest grid spacing in the analysis domain for NOXP. This yielded a radius of influence of 776 m which was set to be constant given the proximity of both radars to the boundary (~5 - 10 km). The grid size was 65 km by 65 km in the horizontal while the vertical grid

levels started at 100 m above ground level (AGL) from the reference point of NOXP[1] since the beam height near the boundary was around this height and extended up to 6 km AGL. This shallow vertical depth was chosen since the boundary and associated air masses were discernible in the lowest scans of each radar (well below 6 km), and it is less computationally expensive. NOXP served as the grid center and grid spacing was 250 m in both the horizontal and vertical dimensions.

During operations on the 28th, NOXP and TTUKa-2 had overlapping scans that included a portion of the preexisting airmass boundary between 2255 and 2302Z. NOXP was located around 5-8 km south of the boundary during this period placing the beam approximately 100 m AGL relative to the surface position of the boundary while TTUKa-2 was 8-10 km north of the boundary also placing the beam around 100 m AGL relative to the boundary's surface position. Using the open-source Pythonic Direct Data Assimilation (PyDDA; Shapiro et al. 2009; Potvin et al. 2012; Jackson et al. 2020) package, a dual-Doppler analysis was performed to determine the two-dimensional horizontal winds across the boundary (the shallow elevation scans of TTUKa-2 did not permit accurate vertical motion estimates).

PyDDA uses the three-dimensional variational (3DVAR) technique to derive the three-dimensional wind field from multiple radars by minimizing a cost function that is comprised of radial velocity observations, mass continuity, and smoothness constraints that users can customize to enhance the resultant wind field (Jackson et al. 2020). Users can also set an initial first-guess wind field using sounding data. The TORUS sounding launched at 2219Z (Fig. 2.10) was the closest to the Tipton supercell's environment in

[1] NOXP and TTUKa-2 had an elevation difference of 10 m with TTUKa-2 at the lower elevation.

space and time, so it was used to initialize the wind field. Constraints used for the calculations are shown in Table 3.4 and follow those used in Potvin et al. (2012).

Table 3.4: PyDDA parameters.

Parameter	**Setting**
C_o (radar)	1
C_m (mass continuity)	30
C_x, C_y, C_z (smooth)	10^{-4}
C_v (vertical vorticity)	10^{-4}
C_b (background)	None
U_t (storm u)	13.5 m s^{-1}
V_t (storm v)	9.4 m s^{-1}
u,v,w initialization	sounding u, sounding v, 0 m s^{-1}

While the typical beam crossing angles used in a dual-Doppler analysis range from 30-150° to minimize errors (Davies-Jones 1979), this case was further limited to 58-120° based on where the two radar beams overlapped. This resulted in a smaller domain, but the dual-Doppler lobes still contained the boundary and the wind fields of the air masses across the boundary (Fig. 3.4).

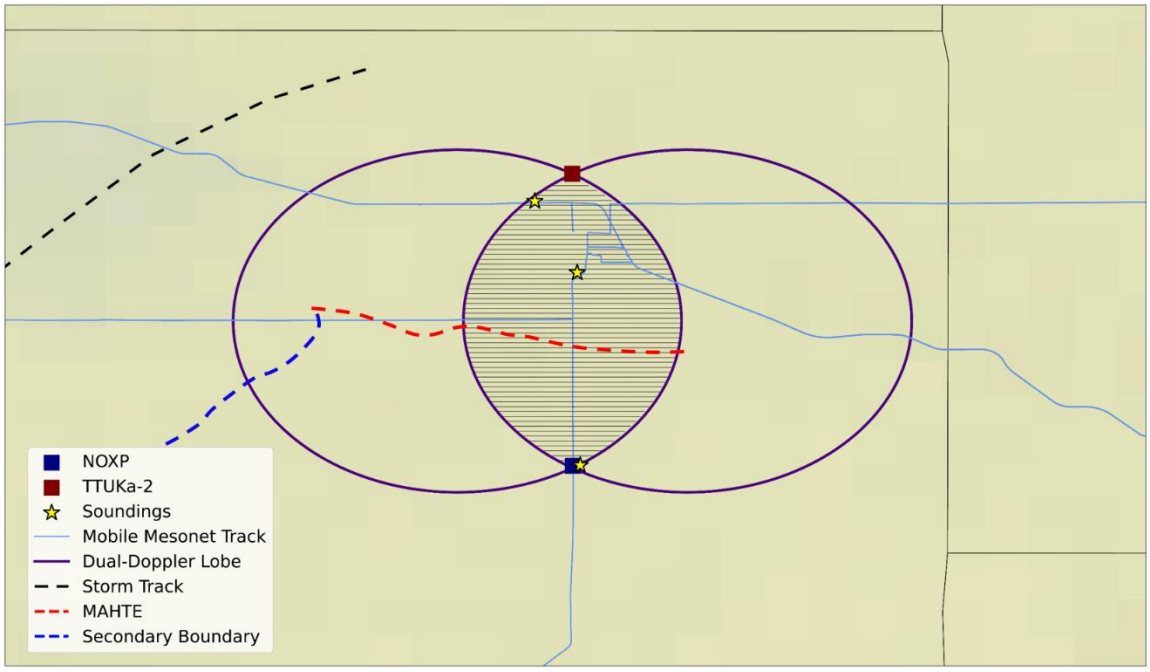

Figure 3.4: Domain for the dual-Doppler analysis. NOXP and TTUKa-2 (dark blue and dark red squares respectively), TORUS soundings (yellow stars), all mobile mesonet tracks (light blue solid lines), the 58-120° beam crossing area of the dual-Doppler analysis domain between NOXP and TTUKa-2 (dark purple rings), storm centroid track for the Tipton supercell (black dashed curve), the MAHTE based on NOXP reflectivity observations (red dashed curve), and the secondary boundary based on NOXP reflectivity observations (blue dashed curve) are shown. NOXP and TTUKa-2 are 16.21 km apart. The striped region indicates where data between the radars cannot be used for the dual-Doppler analysis.

3.3 Storm-scale Analysis

To capture the entire evolution of the Tipton supercell, data from the KUEX WSR-88D radar, located in Blue Hills, NE, were examined in GR2Analyst. This radar is 106 km from Tipton, KS, which places the lowest elevation (0.5°) sweep at approximately 2 km above radar level (ARL) near the Tipton supercell during the TORUS operations on 28 May 2019. NWS warnings and local storm reports are included in this software providing additional details for the timing of tornadogenesis and supplementary confirmation on ground truth associated with radial velocity observations.

GOES-16 visible satellite imagery and 5-minute Kansas Mesonet data (Weather Data Library – Historical Weather 2019) were also used to extrapolate the location and evolution of the synoptic scale warm front throughout 28 May 2019 based on a subjective analysis to aid in interpreting the evolution of the preexisting airmass boundary and the tornadic and nontornadic supercells.

Chapter 4: Results

4.1 Warm Front Progression

As previously discussed, the general environment on 28 May 2019 involved a warm front across north-central Kansas that was the focus for storm initiation. This warm front was the preexisting airmass boundary associated with the MAHTE. The full extent of the possible MAHTE along the warm front is unknown given sparse Kansas mesonet surface stations, but mobile mesonet observations from TORUS support its presence along the portion of the front near the Tipton supercell and nontornadic supercell (Fig. 4.1, see the red box). The development of the MAHTE is not examined in this work, but a more in-depth analysis of the warm front location and progression throughout the afternoon this day was performed to help clarify the full evolution of the two supercells and their interaction with the hypothesized preexisting airmass boundary.

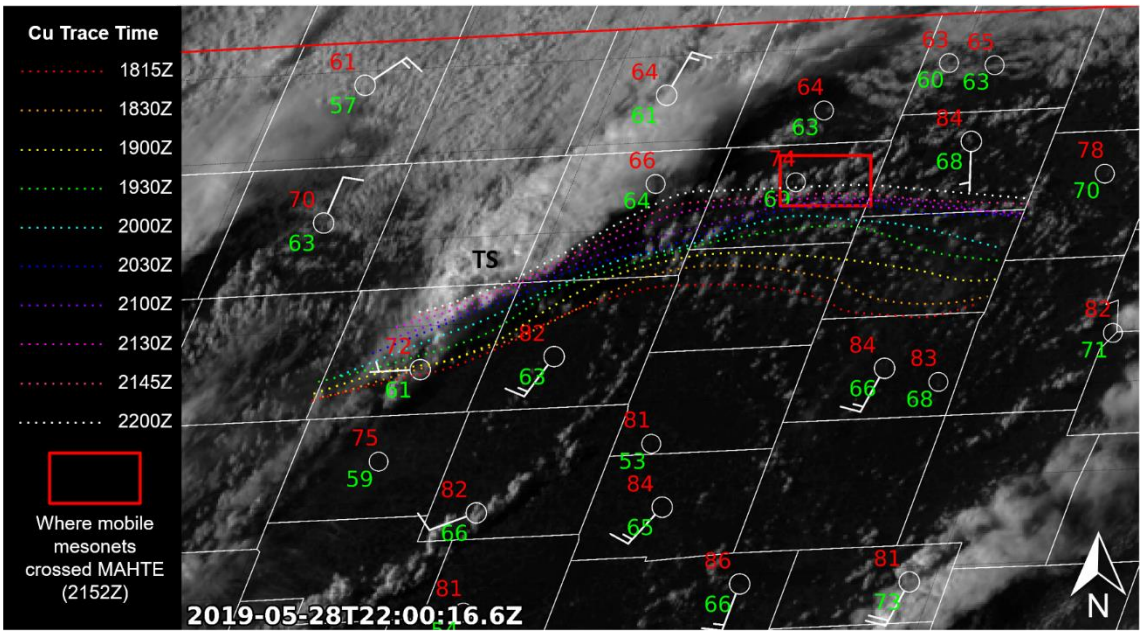

Figure 4.1: GOES-16 visible satellite imagery at 2200Z over north-central Kansas overlaid with dashed lines of different colors representing the subjectively-determined locations of the warm front from 1815Z to 2200Z. Kansas mesonet surface stations plots at 2200Z (white circles) are also overlaid with temperature in Fahrenheit in the top left (red), dewpoint in Fahrenheit in the bottom left (green), and wind barbs in knots. A red box gives the approximate region TORUS mobile mesonets crossed the warm front at 2152Z. Lastly, the bold TS demarcates the location of the Tipton supercell.

Using GOES-16 15-minute visible satellite imagery from 1815-2200Z, the location of the warm front was subjectively analyzed. At 1815Z, the cloud field exhibited a distinct line of cumulus (Cu) disclosing the location of the warm front at this time (see Fig. 2.6a for example of Cu line), and the position of the front was extrapolated in space from this. Around 1900Z, and particularly in the more eastern section of the domain, the line of Cu became less pronounced reducing the accuracy of the subjective analysis in this area. Since mobile mesonets crossed the warm front at 2152Z, these direct observations in combination with the front's earlier movement guided the analysis for times between 1900 and 2200Z.

Figure 4.1 shows traces of the location of the warm front at 15-30 minute intervals between 1815-2200Z. The general warm front orientation gradually changed from meridional to more zonal farther to the east. The zonal section moved faster northward relative to the meridional section throughout the afternoon likely due to more persistent southerly flow observed by the Kansas mesonet surface stations south of this portion of the front. Observations south of the meridional section were more southwesterly reducing the northward advection. North of the zonal section of the warm front, winds were weaker (~ 5 knots) and from the northeast or east but increased (to ~10 knots) with a greater northerly component north of the meridional section.

The Tipton supercell initiated south of the warm front, likely near the low pressure center and intersection of a dryline and cold front while the nontornadic supercell initiated on the warm front near the transition region from meridional to zonal (Fig. 2.6b-d shows the two developing storms). The interaction between the warm front and both supercells will be discussed further in a later section after examining the characteristics of the possible MAHTE in comparison to the warm sector environment and investigating other air masses that were observed near the two storms.

4.2 MAHTE and Warm Air Mass Characteristics

One hypothesis of this work is that a MAHTE formed north of the surface warm front on 28 May 2019. The Kansas mesonet surface observing stations in north-central Kansas at 2200Z revealed the general presence of the warm front (Fig. 4.1) and indicated that dewpoints on the cool side were generally higher than on the warm side, but there was a considerable gap between stations that introduces uncertainty in these results. The

dense observation network provided by TORUS was needed to better characterize these two air masses particularly close to the warm front.

At 2152Z, mobile mesonets crossed the front and observed moderately higher moisture on the cool side (Fig. 4.2). This thermodynamic change was accompanied by a kinematic response involving a wind shift from southerly to northeasterly across the front (Fig. 4.2). Altogether, there was a 2-4 K decrease in temperature (Fig. 4.2a) associated with a 2-3 K increase in dewpoint (Fig. 4.2b) resulting in a θ_e increase of 2-3 K (Fig. 4.2c) on the immediate cool side of the warm front. These observations support the hypothesis that the cool air mass had characteristics of a MAHTE.

To best estimate the boundary-normal width of the MAHTE, Probe-2 observations of θ_e between 2150 and 2154Z were examined (Fig. 4.3), since this mobile mesonet compared best with all three CoMeTs and also continued farther north than them with less time parked. The distance between where Probe-2 crossed the preexisting airmass boundary and where θ_e decreased to below the θ_e of the warm side environment (~350 – 352 K) was calculated. Figure 4.3 demarcates these two points, and the approximate distance between them was estimated to be 12 km. While the intial movement of the warm front was to the north, observations from NOXP later in time (2249Z) indicated the MAHTE was (or the warm front transitioned to) moving to the south and acted more as a cold front. This southward movement was estimated to be around 3 km hr^{-1} and was accounted for when determining the MAHTE width over a 25 minute period. This resulted in an actual estimated width of 13 km. To further investigate the preexisting airmass boundary, observations collected by UAVs in both the MAHTE and warm sector air mass were examined.

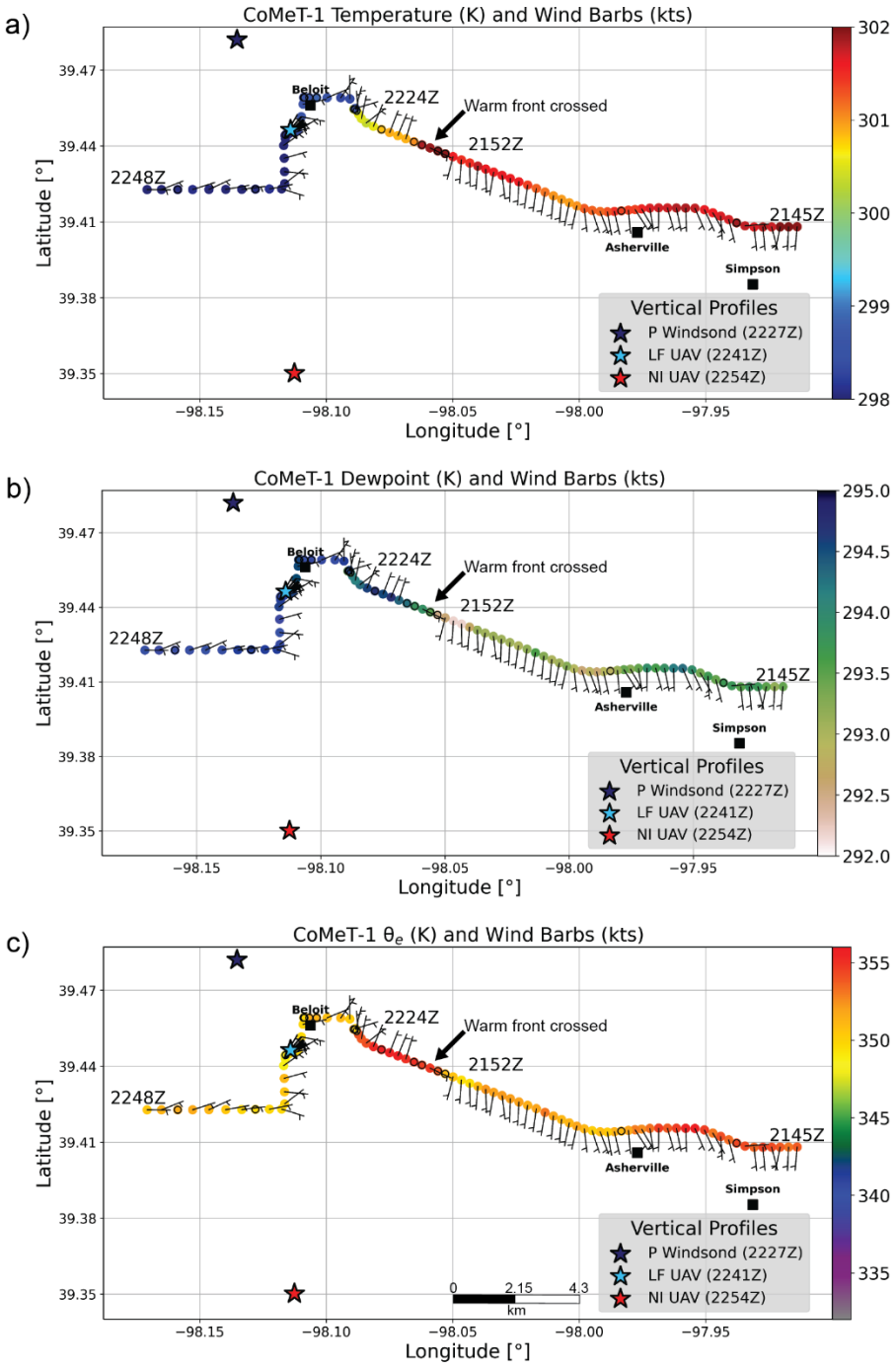

Figure 4.2: CoMeT-1 wind barbs and a) temperature, b) dewpoint, c) equivalent potential temperature in latitude and longitude coordinates (light gray solid lines) from 2145Z to 2248Z (this short time period was selected to best represent the warm front crossing, and the mobile mesonets backtracked over the same roads later in time resulting in overlapping observations). The black arrow highlights where the warm front was crossed at 2152Z, stars represent the location of vertical profiles taken by UAVs later in time and the Windsond® launched by Purdue University (denoted P windsond). Towns are also included (black squares).

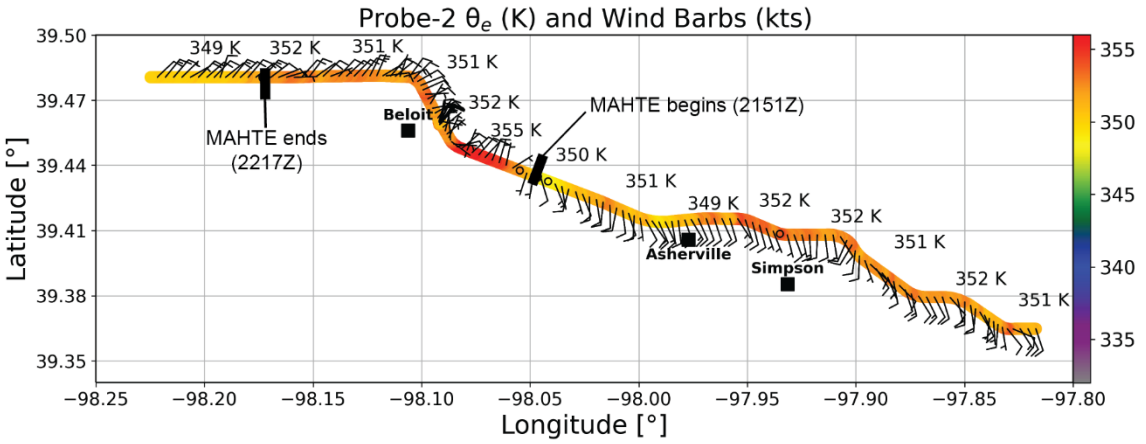

Figure 4.3: Probe-2 wind barbs and equivalent potential temperature in latitude and longitude coordinates (light gray solid lines). The equivalent potential temperature is labeled at different points along the path, and the times when Probe-2 crossed into the MAHTE (2152Z) and out of the MAHTE (2217Z) are demarcated by black lines and labels. Towns are also included (black squares).

The LF UAV and NI UAV were launched within 14 minutes of each other (2241Z and 2254Z respectively) and obtained vertical profiles of the MAHTE and warm air mass respectively (Fig. 4.4). At the surface in Figure 4.4., there is a strong inversion in the warm air mass seen in both the temperature and dewpoint profiles. This inversion suggests there was a decoupling of the near-surface atmosphere from the atmosphere aloft which is likely attributable to anvil shading. This same thermodynamic profile can be seen in a TORUS sounding launched in the warm sector a few kilometers north of the NI UAV at 2255Z (Fig. 4.5). Above this inversion, conditions are closer to what is expected where the MAHTE maintained a cooler temperature and higher moisture relative to the warm air mass (Fig. 4.4). Within the MAHTE, two inversions were evident up to 900 hPa before temperatures began decreasing at a similar rate to the warm air mass. The top of the second inversion is considered the height of the MAHTE and was around 840 m MSL (mean sea level; ~ 400 m AGL). Several meters above the MAHTE,

the dewpoint decreased to the same value as the warm air mass also signifying the vertical depth of the MAHTE.

For the wind profiles, the NI UAV in the warm air mass observed southerly winds in the low levels that increased in speed with height (Fig. 4.4). The MAHTE also exhibited increasing speeds with height but had considerable backing in the lowest levels that transitioned to southerly above the MAHTE (Fig. 4.4) which implies greater vertical wind shear in this air mass. These results align with the model of boundary layer vertical wind profiles expected across boundaries associated with tornadic supercells (Maddox et a. 1980, Fig. 2.1). While this model was developed for meso-α to synoptic scale flow patterns, they compare well to the UAV observations measuring meso-γ scale winds.

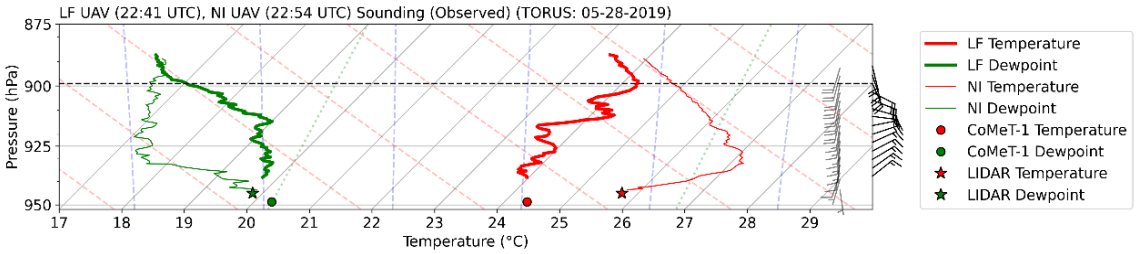

Figure 4.4: 2241 UTC (2254 UTC) LF UAV (NI UAV) sounding on 28 May 2019. The black wind barbs were observed by the LF UAV. The black dashed line denotes the top of the MAHTE. CoMeT-1 and LIDAR surface observations are denoted by circles and stars respectively to compare the UAV observations to the nearest surface observations.

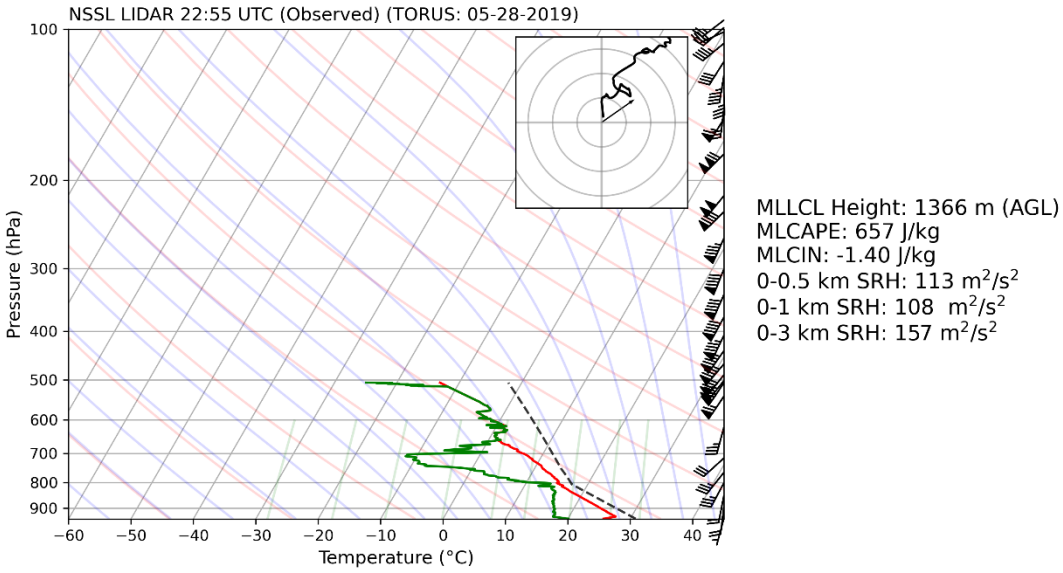

Figure 4.5: 2255 UTC NSSL sounding on 28 May 2019. Hodograph rings are at 10 m s^{-1} intervals. Storm motion vector is based on the Tipton supercell's observed storm motion of 16.5 m s^{-1} from 235°.

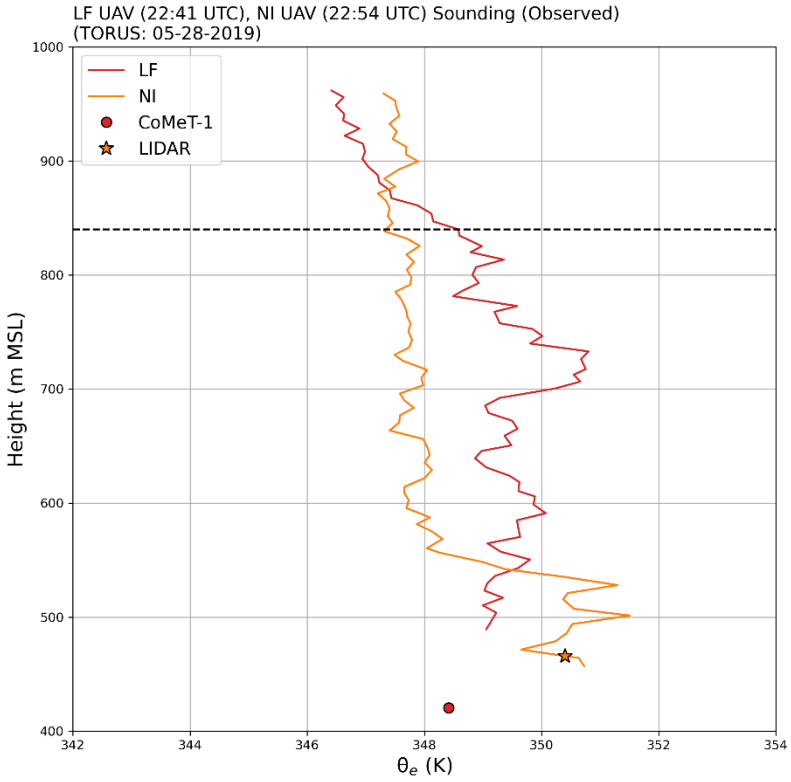

Figure 4.6: 2241 UTC (2254 UTC) LF UAV (NI UAV) vertical profile of equivalent potential temperature. The black dashed line denotes the top of the MAHTE. CoMeT-1 and LIDAR surface observations are denoted by a red circle and orange star respectively to compare the UAV observations to the nearest surface observation.

Looking at vertical profiles of θ_e in both air masses, the hypothesis that the cooler air mass was a MAHTE is supported above the near-surface inversion (Fig. 4.6), but near the surface, θ_e was higher within the warm sector air mass until around 540 m MSL (120 m AGL). Aloft, θ_e was 1-3 K greater throughout the vertical depth of the MAHTE relative to the warm air mass. There was also a "spike" in θ_e of 2 K from around 700-750 m MSL (Fig. 4.6) that corresponded to a brief increase in dewpoint at that same level (Fig. 4.4). Hanft and Houston (2018) found a region of higher θ_e in their simulated MAHTE (Fig. 4.7) that extended from the surface rearward into the cooler air aloft, and it is possible the LF UAV transited a similar feature in this case (refer to the black line in

Fig. 4.7 for the relative location, within the MAHTE on 28 May 2019, where the LF UAV took a vertical profile). θ_e observed at the surface by mobile mesonets was 354 K and decreased to 349 K above the surface (~550-700 m MSL or ~ 130-280 m AGL; Fig. 4.6) and briefly increased to 351 K at 700-750 m MSL (280-330 m AGL).

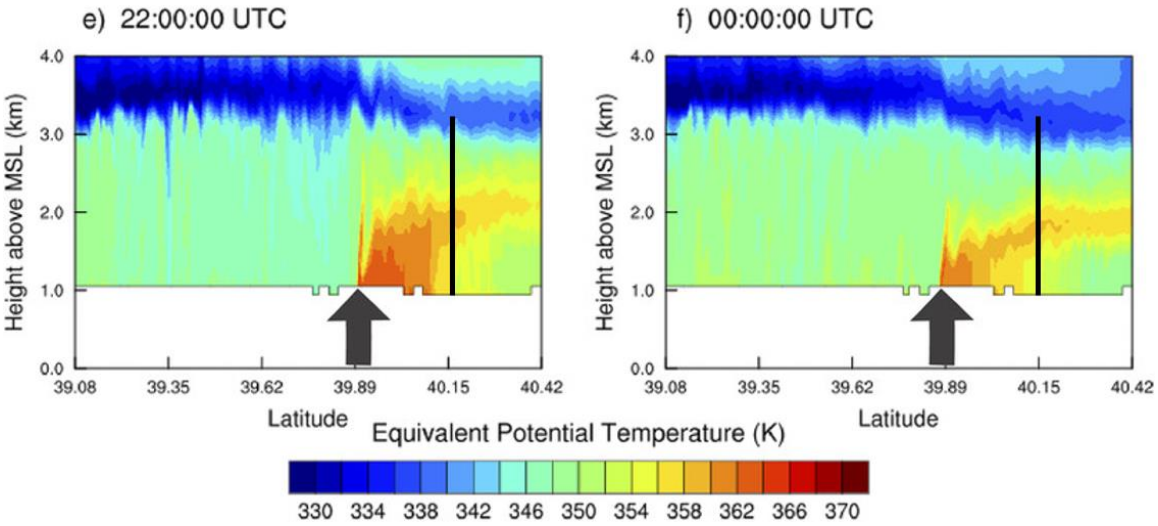

Figure 4.7: Figure 13 taken from Hanft and Houston (2018) of a vertical cross section of equivalent potential temperature through a simulated MAHTE. The figure has been modified with a black line to show the relative location, within the MAHTE on 28 May 2019, the LF UAV took a vertical profile.

These results highlight a limitation in observational studies. Data collected at a single point in space and time makes it difficult to understand when, where, and how the environment is changing particularly near a storm. Influences from changes in solar heating or anvil shading can have small-scale impacts that result in changes in the environment over time, particularly near the surface. Obtaining measurements above the surface is important to map out the conditions within an air mass especially when near surface changes occur. For this case, by the time the UAVs were launched, the surface

conditions no longer indicated a MAHTE was present, but above the surface, the signal remained evident.

Because the vertical profiles collected by the two UAVs represent only the lowest ~600 m of the atmosphere, calculation of parameters that require deep tropospheric data (e.g., CAPE, 0-6 km shear) necessitate combining these profiles with full environmental profile data. The sounding released nearest in space and time to the UAV launches occurred at 2219Z[2] (Fig. 2.8). This sounding was launched 43 km (33 km) south of where the LF UAV (NI UAV) was launched and within the far field environment of the warm sector. Since this profile is not complete, the upper-level environment observed by an earlier sounding at 1931Z (Fig. 2.9) was combined with the 2219Z profile above 9275 m MSL. The LF and NI UAV profiles were embedded at the bottom of the sounding and up to 969 m MSL and 965 m MSL respectively. In addition to these modified soundings, a Windsond® sounding was launched by Purdue University at 2227Z (D. Dawson 2022, personal communication) 4 km north of the LF UAV providing a second profile within the MAHTE (Fig. 4.2, Fig. 4.8). Table 4.1 compares all sounding derived variables between the warm air mass and MAHTE from the different sounding profiles. All sounding derived variables in this study were calculated using SHARPpy (Blumberg et. al 2017).

[2] The 2255Z sounding was convectively contaminated above 650 hPa and did not represent the warm sector environment above this level well.

Table 4.1: Sounding derived variables for the warm air mass (red) and MAHTE/cool air mass (blue).

Sounding Variable	2219/1931Z	2255Z LIDAR	NI UAV + 2219/1931Z	LF UAV + 2219/1931Z	2227Z P windsond
MLLCL Height	1504 m (AGL)	1366 m (AGL)	1419 m (AGL)	1260 m (AGL)	894 m (AGL)
MLCAPE	2686 J kg^{-1}	NA	2768 J kg^{-1}	2745 J kg^{-1}	NA
MLCIN	-2.28 J kg^{-1}	-1.40 J kg^{-1}	-5.14 J kg^{-1}	-23.18 J kg^{-1}	-20.87 J kg^{-1}
0-1 km Bulk Shear	6.7 m s^{-1}	8.2 m s^{-1}	10.3 m s^{-1}	19.5 m s^{-1}	14.9 m s^{-1}
0-3 km Bulk Shear	18 m s^{-1}	12.9 m s^{-1}	22.1 m s^{-1}	31.4 m s^{-1}	24.7 m s^{-1}
0-6 km Bulk Shear	34.5 m s^{-1}	NA	37 m s^{-1}	46.8 m s^{-1}	38.6 m s^{-1}
0-0.5 km SRH	54 m^2 s^{-2}	113 m^2 s^{-2}	101 m^2 s^{-2}	366 m^2 s^{-2}	175 m^2 s^{-2}
0-1 km SRH	80 m^2 s^{-2}	108 m^2 s^{-2}	124 m^2 s^{-2}	390 m^2 s^{-2}	296 m^2 s^{-2}
0-3 km SRH	148 m^2 s^{-2}	157 m^2 s^{-2}	193 m^2 s^{-2}	462 m^2 s^{-2}	461 m^2 s^{-2}

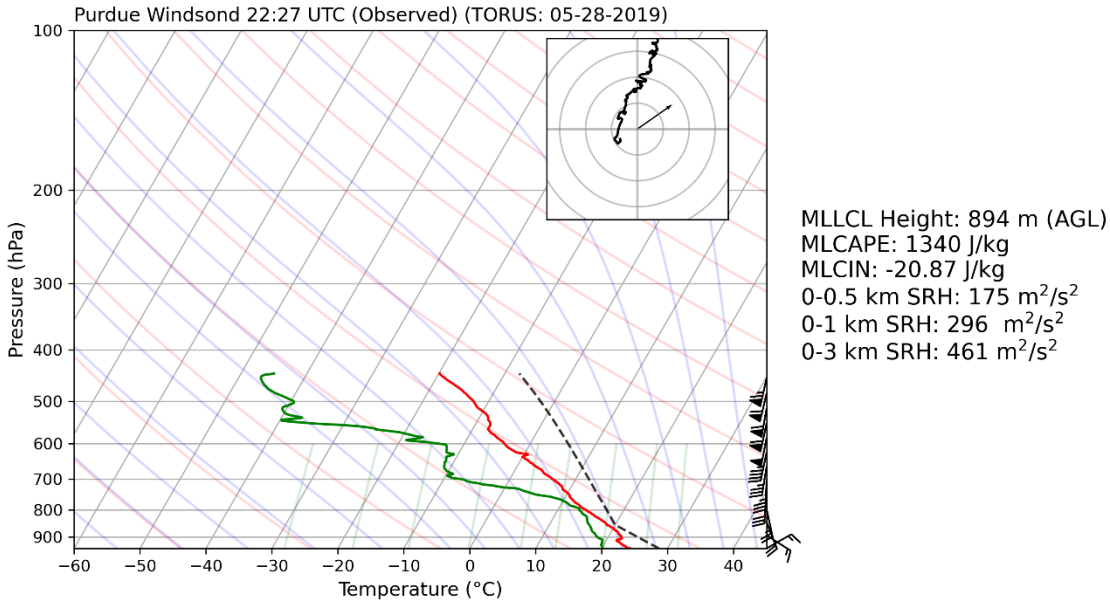

Figure 4.8: Same as Fig. 4.5 except at 2227 UTC from a Purdue University Windsond® sounding.

To summarize, the MAHTE had an LCL height ~160-280 m lower than the warm sector environment. Compared to the 2219/1931Z sounding, the MAHTE had 59 J kg^{-1} more MLCAPE, but when compared to the environmental profile that includes the NI UAV thermodynamic data, the MAHTE had 23 J kg^{-1} less than the warm air mass. For the kinematic data, the bulk shear in the MAHTE was greater than the bulk shear in the warm air mass for all levels and corresponded to greater SRH at all levels shown within the MAHTE (all SRH values are based on the Tipton supercell's observed storm motion of ~16.5 m s^{-1} from 235°). These results are similar to those in Groenmeijer et al. (2011) (Fig. 2.5) since for both cases, the immediate cool side of the boundary had conditions more favorable for tornadic supercells, particularly the kinematic conditions.

Overall, both the warm sector environment and the MAHTE had sufficient instability for deep convection and in particular, supercells. However, the greater low-level SRH within the MAHTE would theoretically promote a stronger and more organized updraft. This in combination with a lower LCL supported by the characteristics of the MAHTE may have been enough to promote tornadogenesis. On the other hand, the nontornadic supercell which formed within the MAHTE never produced robust rotation at the surface. This is potentially due to the MAHTE having higher CIN than the warm air mass and the nontornadic supercell likely not ingesting any parcels from the warm air mass that had almost negligible CIN. Whether or not tornadogenesis would have been less likely if the MAHTE did not form is not a question this work can answer, but a deeper investigation into the role the boundary may have played is carried out through the use of mobile research radars and a dual-Doppler analysis.

a. Dual-Doppler Analysis

From 2255-2302Z, a dual-Doppler analysis was performed to investigate the winds across the preexisting airmass boundary and provide a more spatially coherent understanding of the wind field. Figure 4.8 shows the analysis for three times at 2255Z, 2259Z, and 2302Z at 100 m AGL of the wind field across the preexisting airmass boundary and within the warm air mass and MAHTE (all are east of the Tipton supercell mesocyclone). There were also mobile mesonets and UAVs within or near the dual-Doppler domain that provided in situ wind observations for comparison.

At 2255Z (Fig. 4.9.a), winds within the warm sector were southerly and around 10 knots which compared well with the Kansas mesonet observations south of the preexisting airmass boundary. The NSSL far-field vehicle also observed southerly surface winds around 5 knots in the warm sector just outside of the dual-Doppler lobes. Farther north near the boundary, winds turned cyclonically and weakened. Within the MAHTE, winds were east-northeasterly around 5-10 knots. CoMeT-2, located just east of the analysis domain and immediately behind the boundary, also observed easterly to northeasterly winds around 5 knots at this time. Above the MAHTE at ~975 m MSL (~ 550 m AGL), winds observed by the LF UAV were southerly around 15-20 knots.

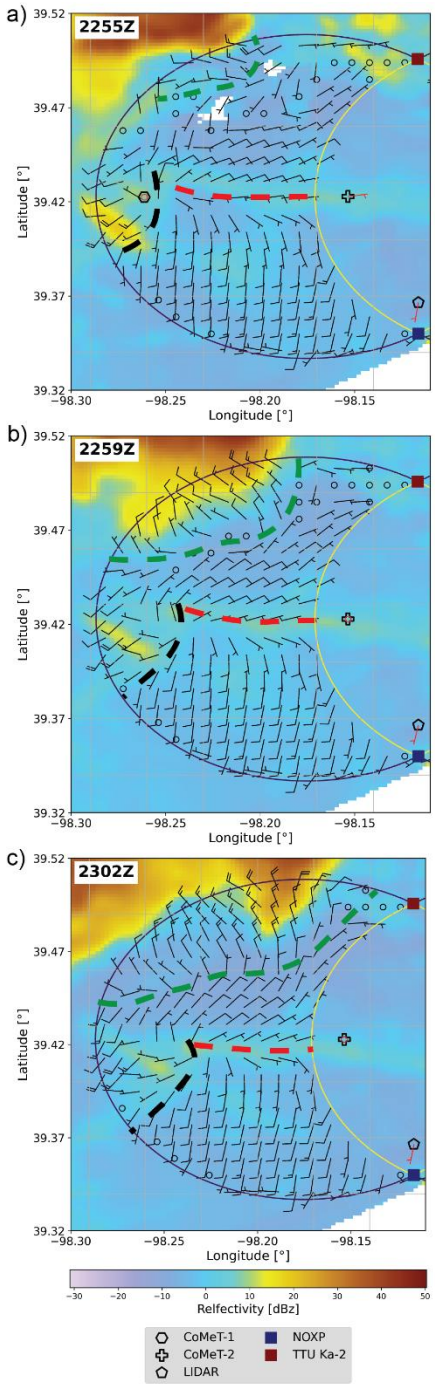

Figure 4.9: Dual-Doppler analysis using NOXP and TTU Ka-2 at a) 2255Z, b) 2259Z, and c) 2302Z. NOXP and TTU Ka-2 scans are from 0-1° with the analysis height at 100 m AGL. Overlaid are surface wind observations from mobile mesonets (red wind barbs), a dashed red curve to demarcate the preexisting airmass boundary, a dashed black curve to demarcate the first outflow from the nontornadic supercell, and a dashed green curve to demarcate a second outflow boundary from the nontornadic supercell. Note: the boundaries extend beyond what is annotated and by 2259Z, CoMeT-1 has traveled west of the domain.

The horizontal wind pattern described above remained persistent for both the warm sector environment south of the preexisting airmass boundary and the MAHTE immediately north of it at 2259Z (Fig. 4.9b) and 2302Z (Fig. 4.9c). However, there are other areas within the wind field that showed distinct wind shifts that became more apparent in the later analysis times. On the western edge of the dual-Doppler lobes, there is a small region of southwesterly winds which initially extended in a small corridor north of the preexisting airmass boundary (Fig. 4.9a). These southwesterly winds became more evident at 2259Z (Fig. 4.9b) and 2302Z (Fig. 4.9c) as this wind field slowly edged eastward. Closer to the surface, in situ observations from CoMeT-1 showed northwesterly winds immediately behind a distinct boundary observed by NOXP (Fig. 4.10c) which shifted to northeasterly 2-3 km behind it (Fig. 4.10d). Aloft, the LF UAV observed a change in winds from southerly to southwesterly at ~975 m MSL (~557 m AGL) as it crossed the same boundary (Fig. 4.11c,d).

This region of southwesterly winds is hypothesized to be associated with a different air mass given a distinct secondary boundary associated with it in NOXP data (Figs. 4.10, 4.11, 4.12, and 4.13) and because it moved to the southeast which is different from the direct southerly movement of the preexisting airmass boundary. The origin of this feature is discussed in the following section as it was in very close proximity to the Tipton supercell.

To the northwest of the corridor of southwesterly winds (Fig. 4.9a), there were northwesterly winds at the edge of the dual-Doppler domain where the RFD of the nontornadic supercell was located. At 2259Z (Fig. 4.9b) and 2302Z (Fig 4.9c), these northwesterly winds moved farther southeast into the dual-Doppler domain indicating

another new air mass was surging towards the preexisting airmass boundary and into the MAHTE. The corridor of southwesterly winds eroded away as this new air mass moved in.

Based on the northwesterly wind direction in this air mass and that it appeared to originate near the nontornadic supercell's RFD, it is presumed to be outflow from the rear flank of the nontornadic storm. Examining in situ data from mobile mesonets CoMeT-1, CoMeT-2, CoMeT-3, and the LF UAV at ~ 270 m AGL between 2310 and 2319Z (Fig. 4.12, Fig. 4.13), a considerable drop in θ_e around 10-12 K was observed indicating a very stable air mass was present. The preexisting airmass boundary also became noticeably deformed by 2319Z (Fig. 4.12d) as the strong outflow merged with it. It is likely that this stable outflow boundary led to the weakening of the Tipton supercell as it moved ahead of the Tipton storm's inflow region. A later section will discuss the evolution of the Tipton supercell relative to this cold outflow boundary to determine how it might have impacted the storm.

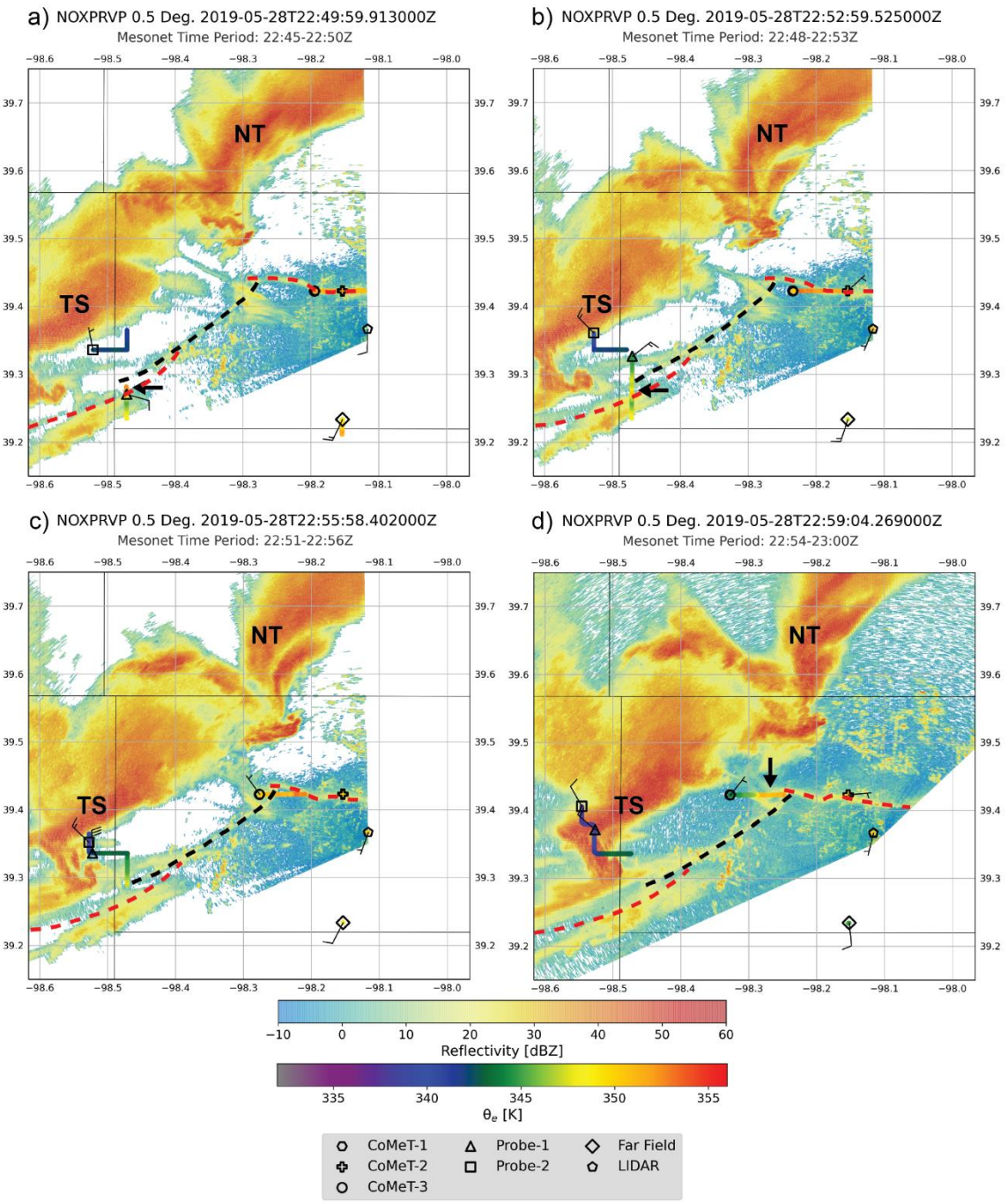

Figure 4.10: NOXP reflectivity between 2250 and 2259Z overlaid with 5 minutes of mobile mesonet observations of equivalent potential temperature and wind barbs for the last observation in the 5 minute period. The preexisting airmass boundary (secondary boundary) is annotated by a red (black) dashed curve. Black arrows in a), b), and c) highlight important thermodynamic changes ahead of and within the air mass behind the secondary boundary. The solid gray lines are associated with the latitude and longitude points, and the thin solid black lines are county lines.

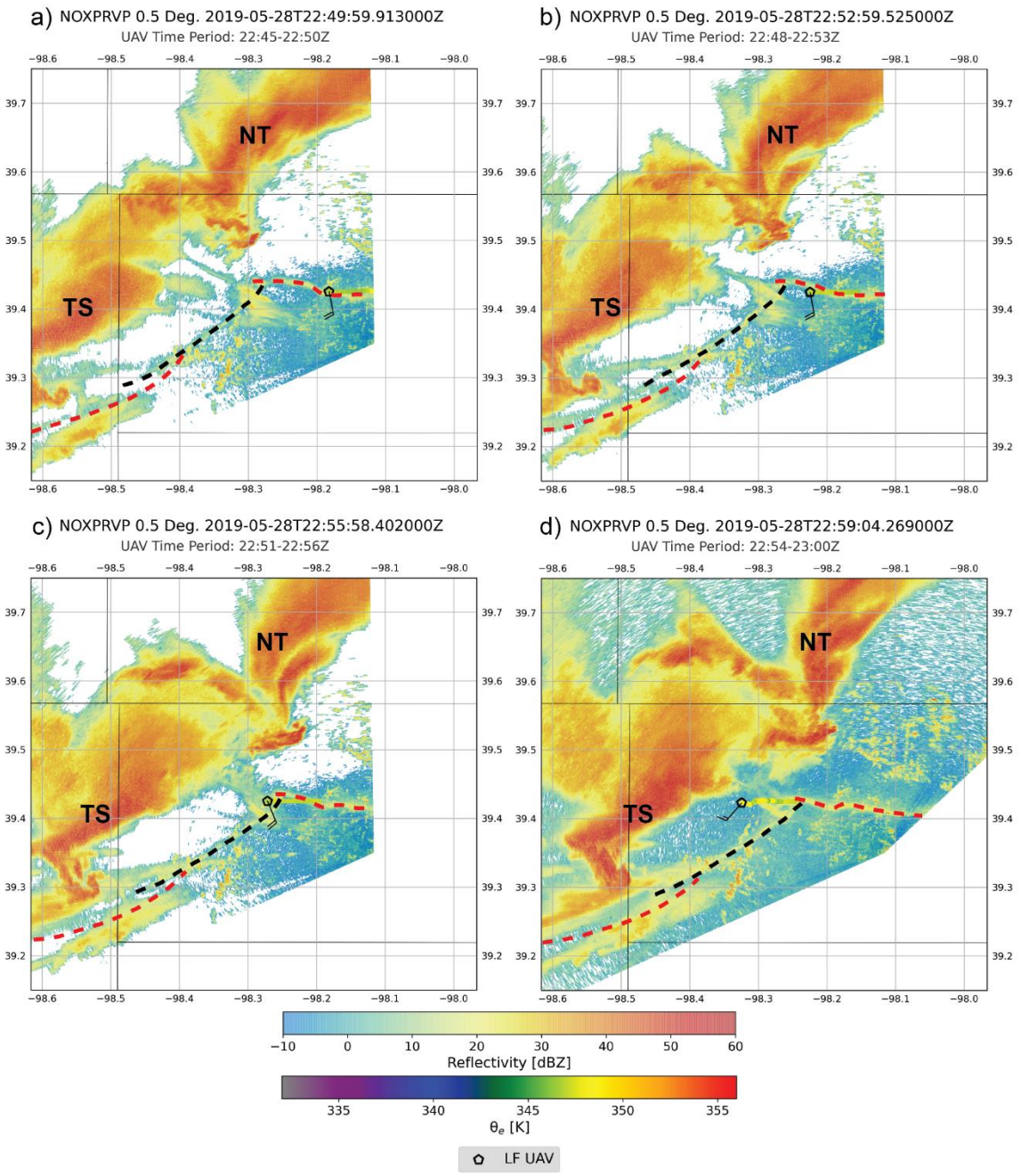

Figure 4.11: Same as 4.10 except with the LF UAV equivalent potential temperature and wind barbs plotted around 550 m AGL.

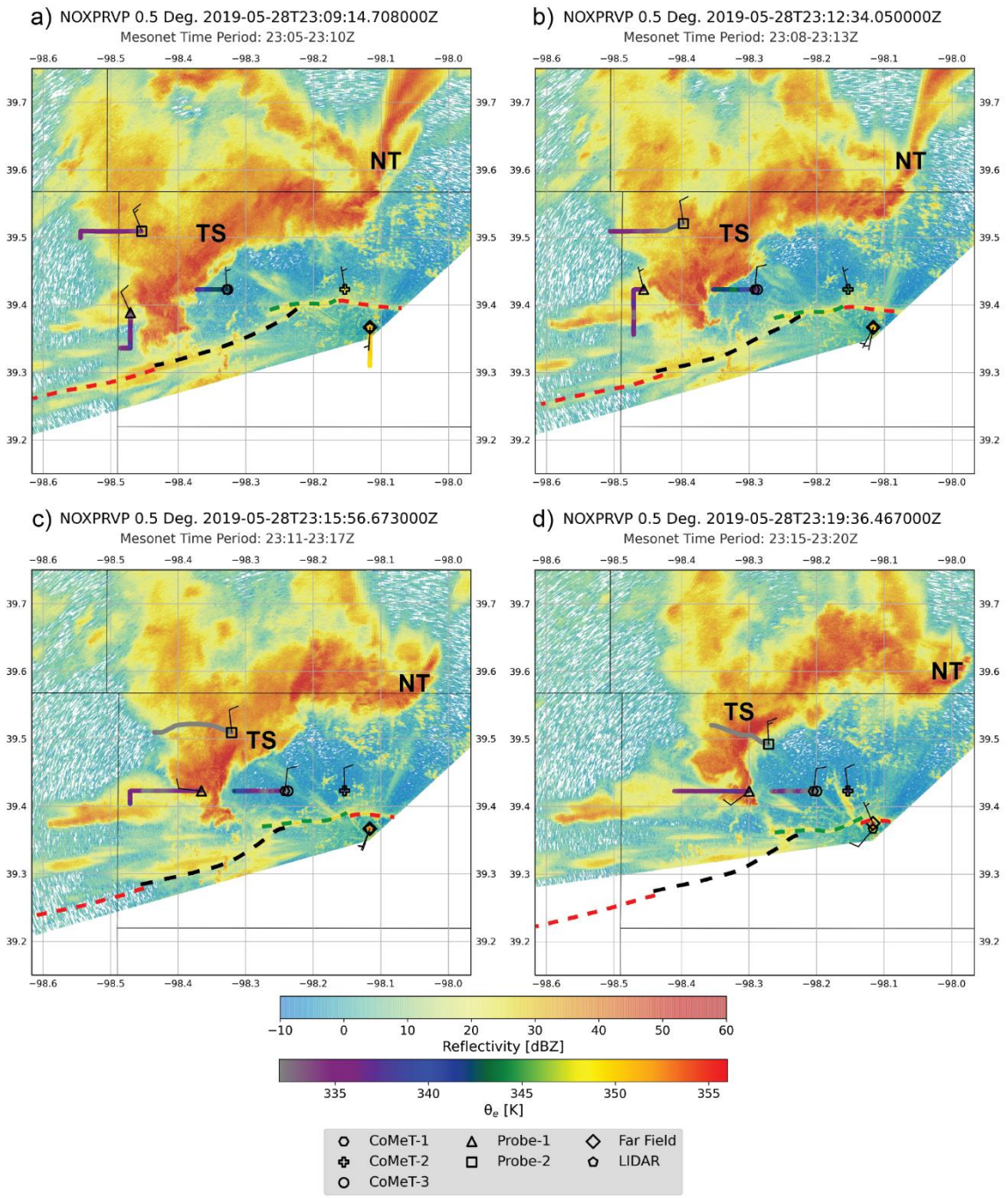

Figure 4.12: Same as 4.10 except between 2309 and 2319Z. A green dashed curve is used to demarcate the second (and stronger) outflow boundary from the nontornadic supercell.

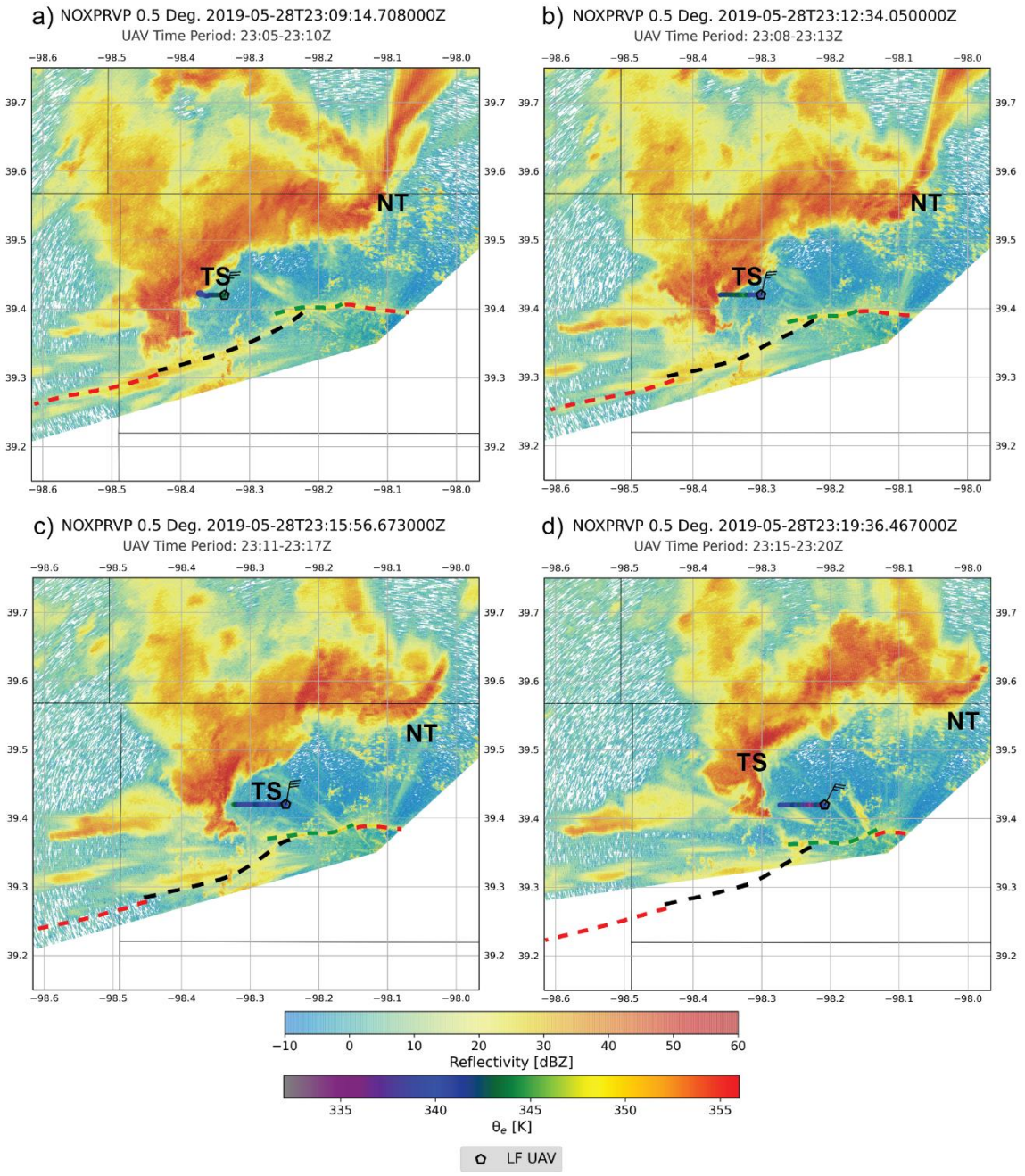

Figure 4.13: Same as 4.11 except between 2249 and 2259Z and around 280 m AGL. A green dashed curve is used to demarcate the second (and stronger) outflow boundary from the nontornadic supercell.

4.3 Origin of the Secondary Boundary

The hypothesis for the origin of the secondary boundary observed by NOXP and mobile mesonets is that it was an outflow boundary from the nontornadic supercell. Figures 4.10 and 4.11 show several time steps between 2249 and 2259Z of NOXP reflectivity data overlaid with in situ observations of θ_e and wind from mobile mesonets and the LF UAV. Probe-1, CoMeT-1, CoMeT-3, and the LF UAV all crossed the secondary boundary but at varying locations. Probe-1 crossed farther south than the other platforms and closer to the Tipton supercell's mesocyclone (Fig 4.9b). Both CoMeTs and the LF UAV transected this boundary near where it intersected with the preexisting airmass boundary (Fig. 4.10c,d; Fig. 4.11c,d). All mobile mesonets observed a moderate decrease in θ_e of 4 K around 2-3 km after passing the reflectivity fine line. Immediately behind the boundary, a corridor of θ_e around 348 K was present before θ_e decreased to 344 K (see black arrow in Fig. 4.10d). CoMeT-1 observed light northwesterly winds in the narrow region of higher θ_e (Fig. 4.10c) and as θ_e decreased to 344 K, winds shifted to a northeasterly direction (Fig 4.10d).

Since the LF UAV was vertically stacked with CoMeT-1 and CoMeT-3 at this time, observations aloft were also obtained (Fig. 4.11). θ_e did not noticeably change aloft as the LF UAV passed over the near-surface position of the secondary boundary, but the winds shifted from southerly to southwesterly farther rearward providing a kinematic indication that the UAV passed over the secondary boundary. There was also a signal in the vertical motion measured by the LF UAV (Fig. 4.14) in two spikes of upward motion corresponding to sudden increases in altitude (Fig. 4.14). The largest upward motion was

around 10 m s^{-1} while the second spike was around 7 m s^{-1} followed by downward motion around -4 m s^{-1} as the LF UAV traveled farther west behind the secondary boundary.

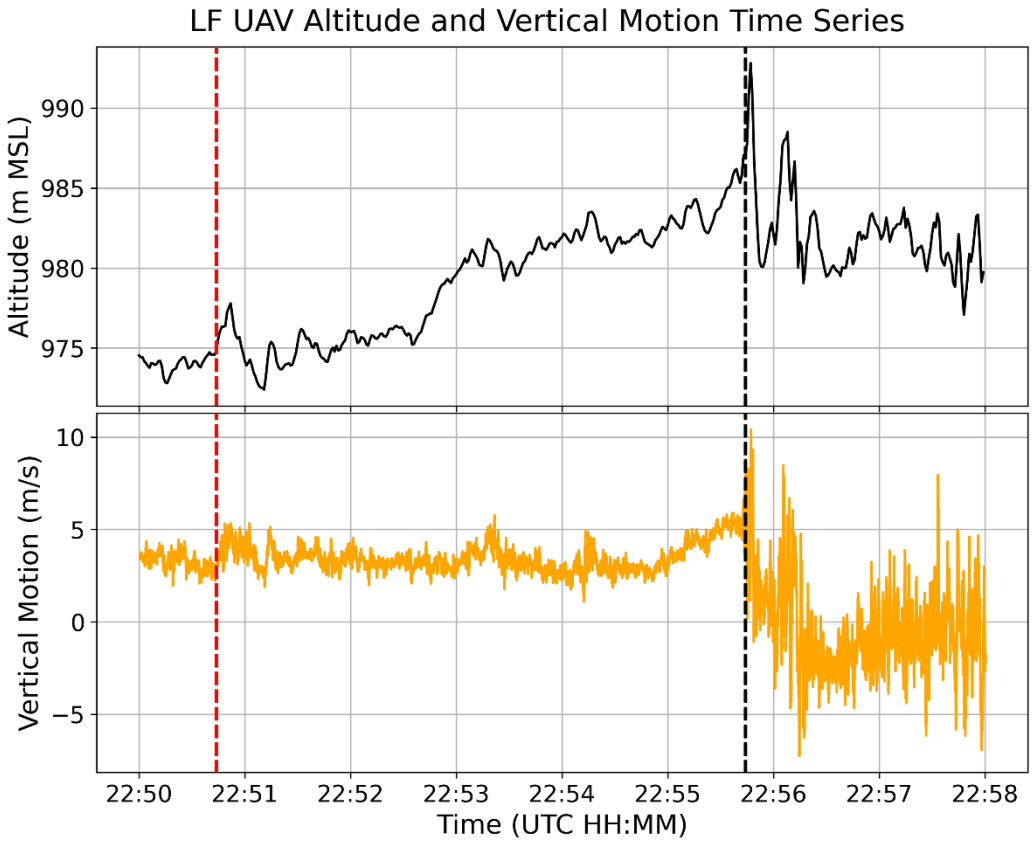

Figure 4.14: LF UAV time series of altitude and vertical motion. The red (black) dashed line marks when the UAV was passing above the MAHTE (above the warm air mass) and over the warm air mass (above the weak outflow boundary/secondary boundary).

Winds measured by Probe-1 within the lower $\boldsymbol{\theta}_e$ air mass behind the boundary were northeasterly as well (Fig. 4.10b) but stronger than the flow observed farther north from the Tipton storm's mesocyclone measured by CoMeT-1. This wind shift occurred immediately after the boundary was crossed after originally being southeasterly in the warm air mass (Fig. 4.10a). The reason Probe-1 did not observe northwesterly flow immediately after crossing the boundary is likely due to the Tipton supercell having a greater influence on the wind field closer to its mesocyclone.

Also noticeable in the Probe-1 observations is a very brief increase in θ_e immediately before Probe-1 crossed the secondary boundary (see black arrow in Fig. 4.10a,b). It is thought that the outflow boundary overtook what was originally the warm front (preexisting airmass boundary) ahead of the Tipton supercell and the small region of higher θ_e before the secondary boundary is remnants of the MAHTE behind the preexisting airmass boundary.

In summary, the hypothesis that the secondary boundary originated as an outflow boundary from the nontornadic supercell is supported by these results. In situ observations at the surface showed a 4 K decrease in θ_e associated with wind shifts typical of outflow boundaries and a distinct fine line in NOXP reflectivity observations. The narrow region of higher θ_e directly behind the secondary boundary where CoMeT-1 crossed was possibly a mixing zone between the outflow air mass and MAHTE as the more stable air overtook part of the preexisting airmass boundary that was ahead of the Tipton supercell. Farther to the south, the outflow boundary likely was still trailing the preexisting airmass boundary and had not yet overtaken the part of the MAHTE in this region. Observations aloft indicated the air mass behind the secondary boundary was likely around a similar shallow height as the MAHTE since no systematic thermodynamic changes occurred where the LF UAV passed over the near-surface boundary.

4.4 Boundary Interaction and Storm Evolution

To infer relationships between the preexisting airmass boundary and the Tipton and nontornadic supercells, an analysis of the subjective location of the boundary over

KUEX WSR-88D observations was performed using GR2Analyst. The boundary position was extrapolated from visible satellite imagery, mobile mesonet observations, and mobile radar observations during the period 2102-2326Z.

Beginning at 2102Z (Fig. 4.15a), the Tipton storm was still south of the warm front (recall it initiated near a triple point south of the warm front) and producing moderate precipitation (40 dBZ) which intensified by 2131Z (Fig. 4.15c) as the storm moved northeast. The first tornado warning was issued around this time prompted by a landspout report which indicates the warm front had possibly been drawn under the storm's updraft near this time. There is also indication of the nontornadic storm developing to the northeast of the Tipton storm where a small region of 30+ dBZ is apparent immediately north of where the warm front was located (Fig. 4.15c). By 2159Z, the Tipton storm showed signs of becoming supercellular with characteristics such as a hook echo and cyclonic rotation in the velocity data at multiple elevation angles (Fig. 4.15e,f; multiple scan heights not shown). By this time, mobile mesonets had crossed the preexisting airmass boundary into the MAHTE ~105 km to the northeast of the Tipton storm. A tornado was also reported on the Tipton supercell not long after at 2204Z but was not the EF2 which formed later.

Based on the analysis, the Tipton supercell started to cross the preexisting airmass boundary around 2131Z (Fig. 4.15c). It is possible the storm began ingesting parcels from both the warm air mass and the MAHTE by this time. This would be consistent with the findings of Laflin and Houston (2012) where trajectories entering a mesocyclone in a simulated supercell originated from both the warm and cool side of a simulated boundary as the storm approached it from the warmer air mass. The nontornadic storm did not

show signs of rotation in the velocity data until ~2215Z indicating it evolved into a supercell, and at 2218Z (Fig. 4.16), there was a subtle indication of the weak outflow (secondary boundary) beginning to emerge from this storm.

Both storms continued to move northeast, and the EF2 tornado associated with the Tipton supercell formed near Waldo, KS around 2223Z (NWS 2021b). This tornado continued until around 2303Z (NWS 2021b), and ground-based mobile radars from TORUS did not begin scanning the supercells until closer to 2250Z. The last set of analysis times between the 2102Z and 2326Z period focus on the latter half when mobile radar data observed the preexisting airmass boundary. The subjective boundary location was modified to include the southward movement of the preexisting airmass boundary and the two outflow boundaries produced by the nontornadic supercell.

By 2250Z (Fig. 4.17a), the Tipton supercell had crossed the section of the warm front that had been overtaken by the secondary boundary associated with the weak outflow from the nontornadic storm. MAHTE air was possibly still present closer to the Tipton storm on this boundary. The nontornadic storm moved farther behind the preexisting airmass boundary and into the cooler air mass compared to earlier times and continued to show classic supercellular radar features (i.e. hook echo and velocity couplet).

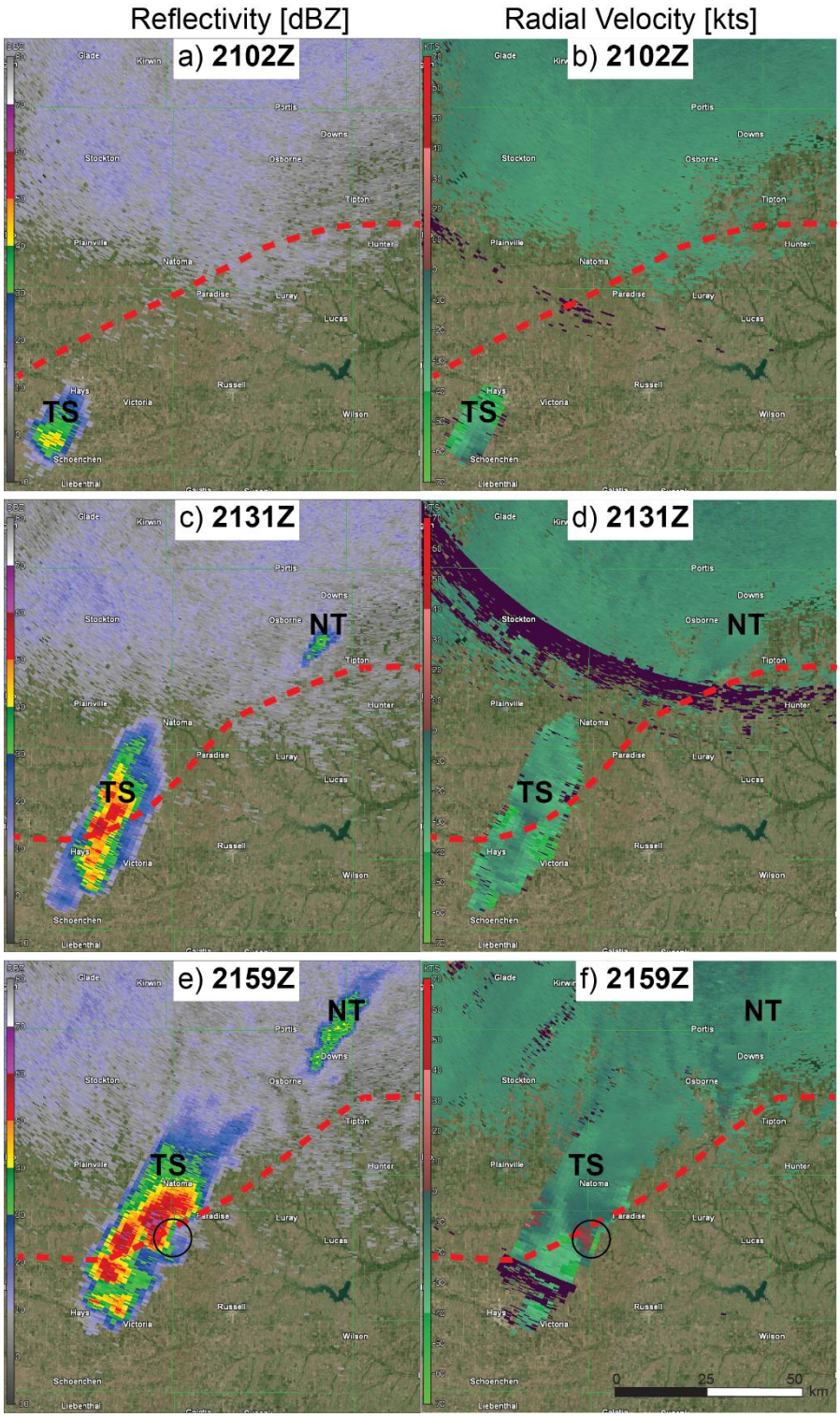

Figure 4.15: KUEX WSR-88D 0.5° scans of the base reflectivity and dealiased radial velocity fields at a)-b) 2102Z, c)-d) 2131Z, and e)-f) 2159Z on 28 May 2019. The red dashed curve represents the warm front location, TS denotes the Tipton supercell, and NT denotes the nontornadic supercell. In e)-f) the black circle highlights the location of the mesocyclone associated with the Tipton supercell.

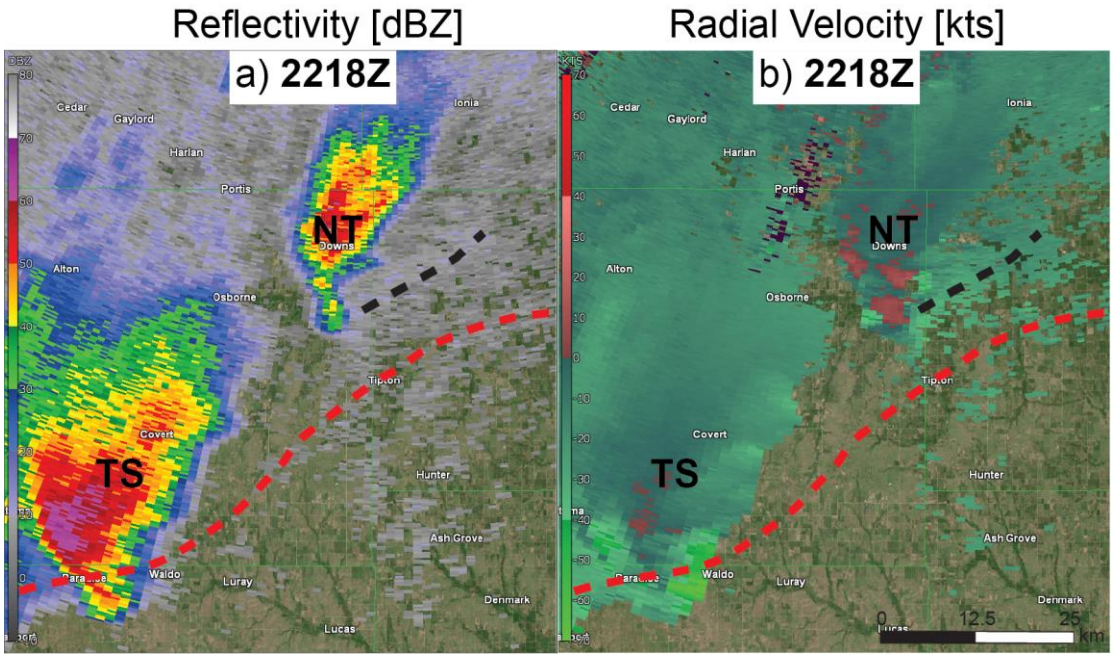

Figure 4.16: Same as Fig. 4.14 except at a)-b) 2218Z. The dashed black curve demarcates the weak outflow that is referred to as the secondary boundary in this work.

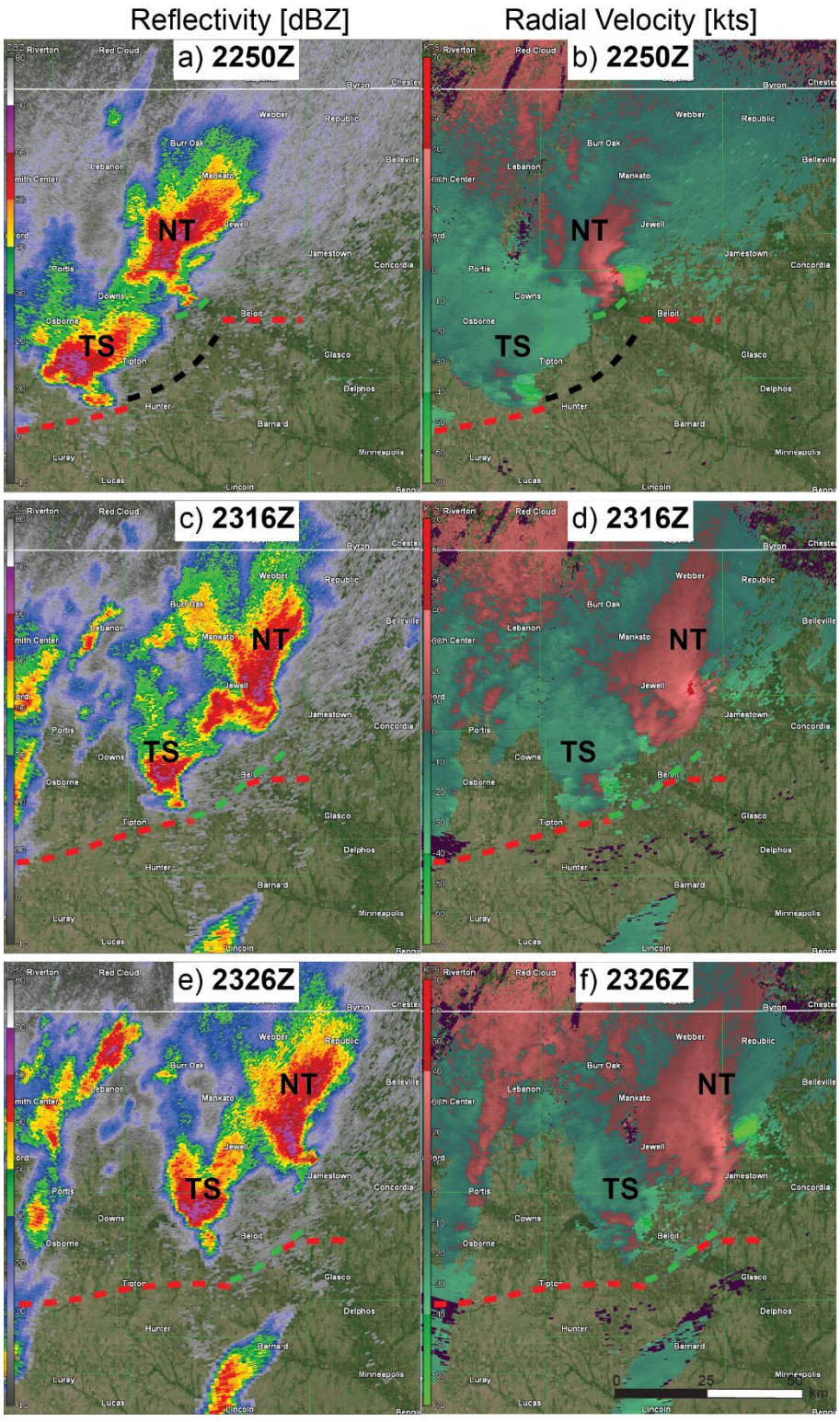

Figure 4.17: Same as Fig. 4.14 except at a)-b) 2250Z, c)-d) 2316Z, and e)-f) 2326Z on 28 May 2019. The dashed black (green) curve demarcates the weak outflow boundary (second and much more stable outflow boundary) that is referred to as the secondary boundary in this work.

By 2316Z (Fig. 4.17c), a second outflow boundary had emerged from the nontornadic supercell which became evident in the KUEX data at this time. The dual-Doppler analysis revealed this outflow formed closer to 2300Z (Fig. 4.8) and the EF2 tornado track ended around 2302Z just south of Tipton, KS (NWS 2021b), possibly as a consequence of storm weakening from this strong outflow. A region of 60+dBZ decreased in size as this outflow surged ahead of the Tipton storm, and by 2326Z, the colder outflow boundary was well ahead of the Tipton storm (Fig. 4.17e). The low-level mesocyclone (exhibited through the radial velocity data) became disorganized and weakened after this time. Meanwhile, the nontornadic supercell maintained an organized low-level mesocyclone throughout this time (Fig. 4.17a,c,e) and after the analysis period.

To summarize, the Tipton storm developed south of the preexisting airmass boundary (warm front) in the warm air mass and became a tornadic supercell as it approached the cooler air mass hypothesized to be characterized as a MAHTE. Based on previous numerical work (Atkins et. al 1999; Laflin and Houston 2012) and the results shown here, a positive relationship is inferred from the interaction of the Tipton supercell and MAHTE. The hypothesis that the MAHTE favorably interacted with the Tipton supercell to promote tornadogenesis is supported for two primary reasons: 1) The MAHTE had qualities more favorable for tornadic supercells, and 2) The Tipton storm was in close proximity to the preexisting airmass boundary and MAHTE, ostensibly resulting in an interaction that supported tornado formation.

With the development of the two outflow boundaries from the nontornadic supercell, there are additional unique complexities to this case, and the full extent of these impacts are difficult to resolve without numerical modeling. Continued work on

supercells interacting with environmental heterogeneities will help clarify supercell behavior and could eventually lead to better understanding of how environmental heterogeneities can impact supercells and vice versa.

Chapter 5: Discussion

This study hypothesized that a MAHTE formed within the cool air mass immediately behind a preexisting airmass boundary on 28 May 2019 and favorably interacted with a tornadic supercell in north-central Kansas. This preexisting airmass boundary was found to be a synoptic-scale warm front and Figure 5.1 provides a schematic of a vertical cross section summarizing the hypothesized structure of the MAHTE using contours of $\boldsymbol{\theta}_e$. Similar to the simulated MAHTE in Hanft and Houston (2018), regions of higher $\boldsymbol{\theta}_e$ extend slightly rearward above the surface. This structure is supported by vertical profiles from UAVs which showed nearly constant $\boldsymbol{\theta}_e$ aloft in the warm sector south of the warm front and higher $\boldsymbol{\theta}_e$ north of the front including a small region of increasing $\boldsymbol{\theta}_e$ aloft.

Altogether, in situ observations from TORUS found higher dewpoints on the immediate cool side of the preexisting airmass boundary that resulted in higher $\boldsymbol{\theta}_e$ values in this air mass relative to the warm air mass. The approximate boundary-normal width of the MAHTE was determined to be around 13 km which falls within the general criteria established for mesoscale phenomena (O(2-200 km)). The vertical depth of the MAHTE was around 400 m, and the conditions of this air mass resulted in similar or greater instability, greater vertical wind shear, and a lower LCL relative to the warm sector environment providing a relatively small region in which conditions were more favorable

for tornadic supercells. The warm air mass showed signs of atmospheric decoupling between the environment at the surface and the environment immediately above the inversion observed in the UAV sounding profiles. This decoupling under the anvil shadow possibly resulted in the absence of mixing allowing for conditions to return to the expected original early morning state where moisture and instability were greater in the warm air mass compared to the cool air mass. This idea is captured in Hanft and Houston (see their Figure 20), but observations above the near-surface inversion still showed a MAHTE was present. It is therefore hypothesized that the MAHTE played a role in promoting tornadogenesis when interacting with the Tipton supercell.

Analysis of the warm front location showed that the Tipton supercell initiated south of the front near a triple point but moved northeast throughout its lifetime and approached the preexisting airmass boundary from the warm side. Given the landspout reports, it is thought that the Tipton storm pulled down the preexisting airmass boundary to south, beginning the interaction between the two. Numerical simulations of supercell-boundary interactions (Atkins et al. 1999; Laflin and Houston 2012) have shown that as supercells approach boundaries from the warm side, parcels ingested into the mid and low-level mesocyclones originate from both the warm and cool air masses. Parcels from the cool air mass experience horizontal vorticity enhancement which can lead to a stronger mesocyclone. In this case the Tipton supercell became tornadic as it moved closer to and along the boundary suggesting it had intensified as it was likely ingesting parcels from the MAHTE.

On this day there was also a nontornadic supercell that formed within this environment but evolved in a different manner than the Tipton supercell. The primary

difference between the two storms is that the nontornadic supercell formed on the warm front and moved into the cool air mass early on in its lifetime. While prior work by Rasmussen et al. (2000), Gilmore and Wicker (2002), Guyer and Ewald (2004), and Groenemeijer et al. (2011) propose that tornadic supercells can still form or maintain themselves when moving into the cool side of a boundary, the shallow depth and width of the MAHTE likely kept the favorable conditions restricted mostly south of the nontornadic storm.

The idea of residence time is also important when considering where the nontornadic storm formed along the boundary. The nontornadic supercell developed closer to where the preexisting airmass boundary had a more zonal orientation while the Tipton supercell interacted with the boundary where it had a more meridional orientation. Both supercells moved to the northeast meaning the Tipton supercell moved more parallel to the boundary than the nontornadic supercell. Studies have found that supercell tornadogenesis is more likely with supercells that move along boundaries (Atkins et al. 1999; Magee and Davenport 2020). The nontornadic supercell also potentially ingested stable parcels farther northeast of the MAHTE while the Tipton supercell ingested parcels from both the warm air mass and MAHTE. The CIN in the MAHTE was also higher than the warm air mass which may have contributed to the nontornadic supercell's inability to produce a tornado.

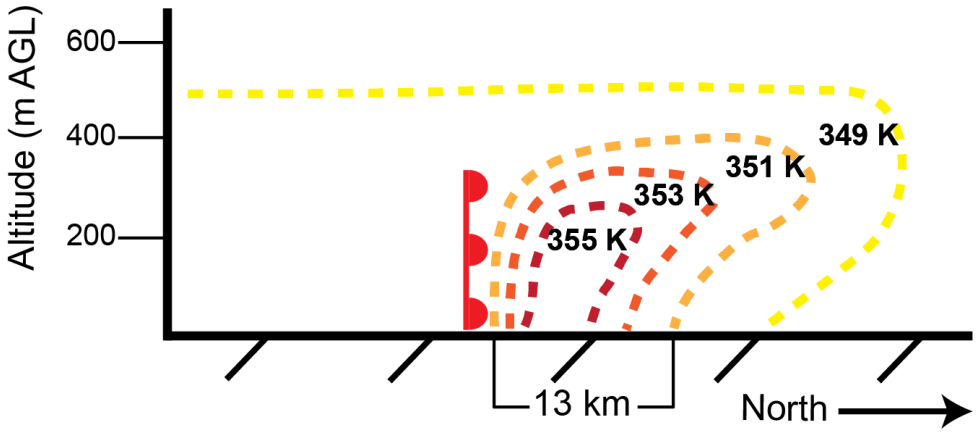

Figure 5.1: Vertical cross section of the hypothesized MAHTE structure. Dashed colored contours represent values of $\boldsymbol{\theta}_e$ and the red scalloped line indicates the location of the warm front (with cooler temperatures towards the north).

Both outflow boundaries from the nontornadic supercell modified the near-storm environment of the Tipton supercell. Ground-based radar data and in situ observations indicated that as the forward flank region of the Tipton supercell started to cross the warm front, the nontornadic supercell produced a weak outflow boundary that moved through the MAHTE and replaced part of the warm front that was ahead of the Tipton storm in its inflow region. Observations within this outflow showed that it had lower $\boldsymbol{\theta}_e$ than both the warm air mass and the MAHTE except for a narrow zone of $\boldsymbol{\theta}_e$ similar to the warm air mass directly behind the boundary. It is proposed that this small region of higher $\boldsymbol{\theta}_e$ air was a mixing zone between the outflow air mass and MAHTE as the more stable air mass collided with the warm front. Figure 5.2 includes conceptual snapshots of what this process generally looked like with the outflow boundary overtaking the warm front. UAV wind data observed above where the outflow boundary and warm front collided exhibited turbulent vertical motion supporting the idea of a narrow mixing zone. Finally, while the weak outflow from the nontornadic supercell did not appear to be detrimental to the Tipton supercell, a second outflow boundary emerged from the

nontornadic supercell that was more stable than the first outflow air mass and surged ahead of the Tipton supercell presumably causing it to weaken and remain nontornadic for the rest of its lifetime.

Overall, this case showed evidence of a possibly constructive interaction between a tornadic supercell and preexisting airmass boundary associated with a MAHTE. A numerical simulation of this case would help to better understand the different processes at play and elucidate the complexities of the case. In general, real cases like the one explored in this work reveal unanswered questions and uncertainties that numerical modeling may be able to test and better deduce what the dominant processes are.

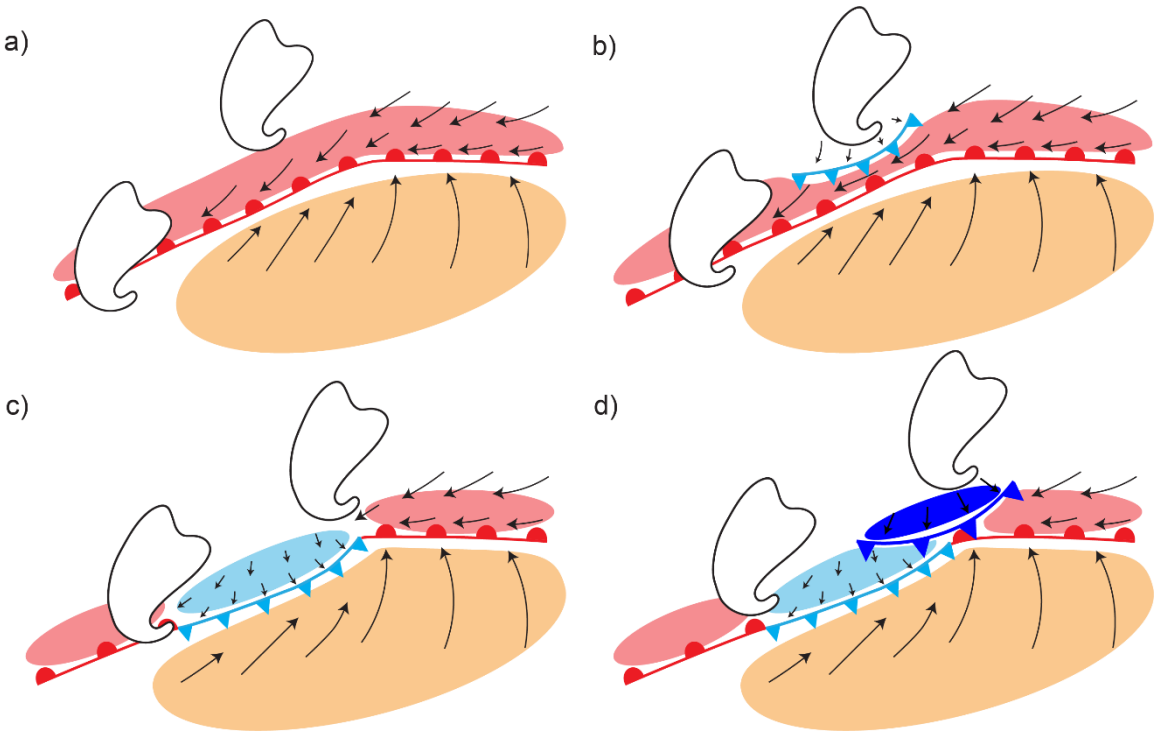

Figure 5.2: Conceptual schematic summarizing the evolution of the 28 May 2019 tornadic and nontornadic supercell interactions with the preexisting airmass boundary (red scalloped curve), and the two outflow boundaries from the nontornadic supercell (the light blue curve with triangles represents the first observed outflow boundary and the dark blue curve with triangles represents the second observed outflow boundary). The black arrows represent the general flow field on both sides of the preexisting airmass boundary and behind the outflow boundaries. The colored shapes represent the general air mass characteristics based on $\boldsymbol{\theta}_e$ with red, beige, light blue, and dark blue corresponding to the MAHTE, warm air mass, first outflow air mass, and second outflow air mass respectively. Two supercells are outlined in black (note: the more northern (southern) storm represents the nontornadic (Tipton) supercell).

Chapter 6: Conclusion

A tornadic supercell interacted with a preexisting airmass boundary on 28 May 2019 in north-central Kansas and was sampled by the 2019 TORUS field campaign which observed a MAHTE on the immediate cool side of a warm front. Mobile mesonets, UAVs, environmental soundings, mobile radars, GOES-16 visible satellite imagery, and Kansas mesonet surface stations were used to investigate the characteristics of the MAHTE and examine the interaction between the preexisting airmass boundary and

tornadic supercell. The MAHTE boundary-normal width and vertical depth were estimated to be ~ 13 km and ~ 400 m AGL respectively with a max θ_e of 355 K observed directly north of the warm front. The higher θ_e in the cooler air mass corresponded to greater instability within the MAHTE and a lower LCL when compared to the warm sector environment. Analysis showed northeasterly winds at low-levels within the MAHTE which resulted in greater vertical wind shear relative to the warm air mass. Altogether, the MAHTE environment was generally more favorable for tornadic supercells.

The evolution of a nontornadic supercell was also investigated as it modified the environment of the tornadic supercell after producing two outflow boundaries. This supercell formed north of the warm front in the MAHTE and progressed into the cool air throughout its life. As the tornadic supercell approached the warm front from the warm side, it intensified and became tornadic. The nontornadic supercell then produced a weak outflow boundary that gradually moved southeast and collided with the warm front replacing the MAHTE with a slightly cooler and drier air mass. Not long after, this same storm produced a stronger second outflow boundary that surged through the tornadic supercell's inflow region causing it to weaken.

This work is an example of the complexities environmental heterogeneities introduce when trying to understand and generalize supercell behavior. While forecasting supercell environments days in advance is relatively straightforward, the exact location and evolution of a supercell is challenging to predict in advance. This becomes even more difficult when supercells interact with environmental heterogeneities such as preexisting airmass boundaries or other nearby supercells. In-depth observational

analyses such as this one are also limited in their ability to fully understand every environmental contribution to the evolution of a supercell. Generally, in situ observations do not provide enough coverage to capture heterogeneities well in the near-storm environment since each observation is restricted in space and time.

Some examples of limitations in this work include the sampling strategy implemented on TORUS which focused more on internal supercell boundaries. Only one transect through the entirety of the MAHTE was performed before the Tipton supercell likely interacted with it. It is unknown if the MAHTE actually extended down the length of the front to the Tipton storm particularly when the nontornadic outflow boundary overtook the preexisting airmass boundary. By the time the Tipton storm could have ingested parcels from the MAHTE, environmental changes could have occurred due to the effects of anvil shading or microscale processes we are unable to capture with the observational tools available. This was seen in the UAV vertical profiles which indicated a decoupling of the near-surface environment from the environment aloft. Surface observations suggested the MAHTE had dissipated but aloft the signal persisted.

Some remaining questions from this study include: Did the MAHTE characteristics notably change by the time the Tipton supercell was close enough to interact with this air mass? At what point did the surface conditions within the MAHTE and warm air mass change while conditions aloft remained relatively the same? Did conditions aloft up to the height of the MAHTE remain the same? Additional observations such as vertical profiles from the UAVs when the mobile mesonets first crossed the preexisting airmass boundary would have helped to answer these questions. Future work for this case involves replicating this environment in a series of numerical

simulations that compare how the tornadic supercell evolves when i) the environment is homogenous, ii) when the warm front has typical conditions with the cooler side having drier air, and iii) when the warm front has the MAHTE on the cool side. These simulations could help determine if the MAHTE was needed to produce a tornado in an environment already supportive for supercells.

Chapter 7: Bibliography

Atkins, N. T., M. L. Weisman, and L. J. Wicker, 1999: The influence of preexisting boundaries on supercell evolution. *Mon. Wea. Rev.*, **127**(12), 2910-2927, https://doi.org/10.1175/1520-0493(1999)127<2910:TIOPBO>2.0.CO;2.

Barnes S., 1964: A Technique for maximizing details in numerical weather map analysis. *J. Appl. Meteor. Climatol.*, **3**(4), 396-409. https://doi.org/10.1175/15200450(1964)003<0396:ATFMDI>2.0.CO;2.

Blumberg, W. G., K. T. Halbert, T. A. Supinie, P. T. Marsh, R. L. Thompson, and J. A. Hart, 2017: SHARPpy: An open-source sounding analysis toolkit for the atmospheric sciences. *Bull. Amer. Meteor. Soc.*, **98**, 1625-1636, https://doi.org/10.1175/BAMS-D-15-00309.1.

Burgess, D., Mansell, T., Reinhart, A., 2020: NOXP Radar Data: Version 1.0. UCAR/NCAR - Earth Observing Laboratory, accessed 2 February 2021, https://doi.org/10.26023/BX3D-5PBJ-6P0A.

Davies-Jones, R. P., 1979: Dual-Doppler radar coverage area as a function of measurement accuracy and spatial resolution. *J. Appl. Meteor.*, **18**, 1229-1233. https://doi.org/10.1175/1520-0450-18.9.1229.

Elston, J. S., J. Roadman, M. Stachura, B. Argrow, A. Houston, and E. W. Frew, 2011: The tempest unmanned aircraft system for in situ observations of tornadic supercells: Design and VORTEX2 flight results. *J. Field Rob.*, **28**, 461–483, https://doi.org/10.1002/rob.20394.

Frew, E., et al., 2020: University of Colorado RAAVEN sUAS Data: Version 1.0. UCAR/NCAR - Earth Observing Laboratory, accessed 2 February 2021, https://doi.org/10.26023/FJD8-VMV2-XW0Y.

Gilmore, M. S., & Wicker, L. J., 2002: Influences of the local environment on supercell cloud-to-ground lightning, radar characteristics, and severe weather on 2 June 1995. *Mon. Wea. Rev.*, **130**, 2349-2372, https://doi.org/10.1175/1520-0493(2002)130<2349:IOTLEO>2.0.CO;2.

Groenemeijer, P., U. Corsmeier, and Ch. Kottmeier, 2011: The development of tornadic storms on the cold side of a front favoured by local enhancement of moisture and CAPE. *Atmos. Res.*, **100**, 765-781, https://doi.org/10.1016/j.atmosres.2010.10.028.

Guyer, J. L., and R. Ewald, 2004: Record hail event—Examination of the Aurora, Nebraska supercell of 22 June 2003. *22nd Conf. on Severe Local Storms*, Hyannis, MA, Amer. Meteor. Soc., 11B.1, https://ams.confex.com/ams/11aram22sls/techprogram/paper_82087.htm.

Hanft, W., and A. L. Houston, 2018: An observational and modeling study of mesoscale air masses with high theta-E. *Mon. Wea. Rev.*, **146**(8), 2503-2524, https://doi.org/10.1175/MWR-D-17-0389.1.

Helmus, J.J. and S.M. Collis, 2016: The Python ARM Radar Toolkit (Py-ART), a library for working with weather radar data in the Python programming language. *J. of Open Rea. Software*, **4**(1), e25, http://doi.org/10.5334/jors.119.

Honda, T., and T. Kawano, 2016: A possible mechanism of tornadogenesis associated with the interaction between a supercell and an outflow boundary without horizontal shear. *J. Atmos. Sci.*, **73**, 1273-1292, https://doi.org/10.1175/JAS-D-14-0347.1.

Houston, A. L., B. Argrow, M. C. Coniglio, E. W. Frew, E. N. Rasmussen, C. C. Weiss, and C. L. Ziegler, 2020: Targeted Observation by Radars and UAS of Supercells (TORUS): Summary of the 2019 field campaign. *Severe Local Storms Symp.*, Boston, MA, Amer. Meteor. Soc., 1.3, https://ams.confex.com/ams/2020Annual/webprogram/Paper369999.html.

Houston, A., Axon, K., Erwin, A., 2021a: UNL Combined Mesonet and Tracker (CoMeT-1) Mobile Mesonet Data: Version 2.1. UCAR/NCAR - Earth Observing Laboratory, accessed 2 February 2021, https://doi.org/10.26023/B967-JN6J-AY03.

Houston, A., Axon, K., Erwin, A., 2021b: UNL Combined Mesonet and Tracker (CoMeT-2) Mobile Mesonet Data: Version 2.1. UCAR/NCAR - Earth Observing Laboratory, accessed 2 February 2021, https://doi.org/10.26023/JWPF-089R-8J0B.

Houston, A., Axon, K., Erwin, A., 2021c: UNL Combined Mesonet and Tracker (CoMeT-3) Mobile Mesonet Data: Version 2.1. UCAR/NCAR - Earth Observing Laboratory, accessed 2 February 2021, https://doi.org/10.26023/DCF0-DW77-H20Q.

Jackson, R., S. Collis, T. Lang, C. Potvin, and T. Munson, 2020: PyDDA: A Pythonic Direct Data Assimilation framework for wind retrievals. *J. of Open Rea. Software*, **8**, 20, http://doi.org/10.5334/jors.264.

Johns, R. H., C. Broyles, D. Eastlack, H. Guerrero, and K. Harding, 2000: The role of synoptic patterns and temperature and moisture distribution in determining the locations of strong and violent tornado episodes in the North Central United States: A preliminary examination. Preprints, *20th Conf. on Severe Local Storms*, Orlando, FL, Amer. Meteor. Soc., 489–492.

Laflin, J. M. and A. L. Houston, 2012: A modeling study of supercell development in the presence of a preexisting airmass boundary. *Electronic J. Severe Storms Meteor.*, **7**(1), 1–29.

Maddox, R. A., L. R. Hoxit, and C. F. Chappell, 1980: A study of tornadic thunderstorm interactions with thermal boundaries. *Mon. Wea. Rev.*, **108**, 332-336, https://doi.org/10.1175/1520-0493(1980)108<0322:ASOTTI>2.0.CO;2.

Magee, K. M., and C. E. Davenport, 2020: An observational analysis quantifying the distance of supercell-boundary interactions in the Great Plains. *J. Operational Meteor.*, **8** (2), 15-38, doi: https://doi.org/10.15191/nwajom.2020.0802.

Markowski, P. M., E. N. Rasmussen, and J. M. Straka, 1998: The occurrence of tornadoes in supercells interacting with boundaries during VORTEX-95. *Wea. Forecasting*, **13**, 852-859, https://doi.org/10.1175/1520-0434(1998)013<0852:TOOTIS>2.0.CO;2.

Markowski, P. M., and S. Richardson, 2009: Tornadogenesis: our current understanding, forecasting considerations, and questions to guide future research. *Atmos. Rea.*, **93**, 3-10, https://doi.org/10.1016/j.atmosres.2008.09.015.

Miloshevich, L. M., A. Paukkunen, H. Vömel, and S. J. Oltmans, 2004: Development and validation of a time-lag correction for Vaisala radiosonde humidity measurements. *J. Atmos. Oceanic Technol.*, **21**, 1305-1327, https://doi.org/10.1175/1520-0426(2004)021<1305:DAVOAT>2.0.CO;2.

NWS, 2021a: National Weather Service Birmingham AL reduced tornado warning false alarm rate by 31% since April 2011. Accessed 02 December 2021, https://www.weather.gov/bmx/research_falsealarms.

NWS, 2021b: May 26-28, 2019: Tornadoes on 3-Consecutive Days! (including an EF-2 in KS). Accessed 02 December 2021, https://www.weather.gov/gid/latemay2019tors.

Pauley, P. M. and X. Wu, 1990: The theoretical, discrete, and actual response of the Barnes objective analysis scheme for one- and two-dimensional fields. *Mon. Wea. Rev.*, **118**, 1145-1164, https://doi.org/10.1175/1520-0493(1990)118<1145:TTDAAR>2.0.CO;2.

Potvin, C.K., A. Shapiro, and M. Xue, 2012: Impact of a vertical vorticity constraint in variational dual-Doppler wind analysis: Tests with real and simulated supercell data. *J. Atmos. Oceanic Technol.*, **29**, 32–49, https://doi.org/10.1175/JTECH-D-11-00019.1.

Rasmussen, E. N., S. Richardson, J. M. Straka, P. M. Markowski, and D. O. Blanchard, 2000: The association of significant tornadoes with a baroclinic boundary on 2 June 1995. *Mon. Wea. Rev.*, **128**, 174-191, https://doi.org/10.1175/1520-0493(2000)128<0174:TAOSTW>2.0.CO;2.

Riganti, C. J., and A. L. Houston, 2017: Rear-flank outflow dynamics and thermodynamics in the 10 June 2010 Last Chance, Colorado, supercell. *Mon. Wea. Rev.*, **145**(7), 2487-2504, https://doi.org/10.1175/MWR-D-16-0128.1.

Shapiro, A., C.K. Potvin, and J. Gao, 2009: Use of a vertical vorticity equation in variational dual-Doppler wind analysis. *J. Atmos. Oceanic Technol.*, **26**, 2089–2106, https://doi.org/10.1175/2009JTECHA1256.1.

Smith, E., Coniglio, M., 2019: NSSL Mobile Lidar Data: Version 1.0. UCAR/NCAR - Earth Observing Laboratory, accessed 2 February 2021, https://doi.org/10.26023/EVYG-3VV6-YC0E.

Thompson, R. L., Edwards, R., Hart, J. A., Elmore, K. L., and Markowski, P., 2003: Close proximity soundings within supercell environments obtained from the rapid update cycle. *Wea. Forecasting*, **18**, 1243-1261, https://doi.org/10.1175/1520-0434(2003)018<1243:CPSWSE>2.0.CO;2.

Weather Data Library – Historical Weather, 2019: Kansas Mesonet. Kansas State University, accessed 15 March 2022, https://mesonet.k-state.edu/weather/historical/.

Wheatley, D. M., and R. J. Trapp, 2008: The effect of mesoscale heterogeneity on the genesis and structure of mesovortices within quasi-linear convective systems. *Mon. Wea. Rev.*, **136**(11), 4220-4241, https://doi.org/10.1175/2008MWR2294.1.

Wade, A. R., M. C. Coniglio, and C. L. Ziegler, 2018: Comparison of near- and far-field supercell inflow environments using radiosonde observations. *Mon. Wea. Rev.*, **146**, 2403–2415, https://doi-org.libproxy.unl.edu/10.1175/MWR-D-17-0276.1.

Waugh, S., 2020a: NSSL Mobile Mesonet Data: Version 1.1. UCAR/NCAR - Earth Observing Laboratory, accessed 2 February 2021, https://doi.org/10.26023/2Y87-XEEB-7W13.

Waugh, S., 2020b: NSSL Mobile Quality Controlled (QC) Radiosonde Data: Version 1.0. UCAR/NCAR - Earth Observing Laboratory, accessed 2 February 2021, https://doi.org/10.26023/MDEM-SG4J-5P10.

Weiss, C., and A. Schueth, 2019. Texas Tech University Ka Band (TTUKA) Mobile Radar Data: Version 1.2. UCAR/NCAR - Earth Observing Laboratory, accessed 2 February 2021, https://doi.org/10.26023/9QY1-9TWD-TB08.

Wicker, L. J., and R. B. Wilhelmson, 1995: Simulation and analysis of tornado development and decay within a three-dimensional supercell thunderstorm, *J. Atmos. Sci.*, **52**(15), 2675-2703, https://doi.org/10.1175/1520-0469(1995)052<2675:SAAOTD>2.0.CO;2.

Wurman, J., D. Dowell, Y. P. Richardson, P. M. Markowski, E. Rasmussen, D. Burgess, L. Wicker, and H. B. Bluestein, 2012: The Second Verification of the Origins of Rotation in Tornadoes Experiment: VORTEX2. *Bull. Amer. Meteor. Soc.*, **93**, 1147–1170, https://doi.org/10.1175/BAMS-D-11-00010.1.